

Mechanisms of Dispersion in a Porous Medium

M. Dentz¹†, M. Icardi² and J. J. Hidalgo¹

¹Spanish National Research Council, IDAEA-CSIC, c/ Jordi Girona 18, 08034 Barcelona, Spain

²Warwick Mathematics Institute, University of Warwick, CV4 7AL Coventry, UK

(5 March 2018)

This paper studies the mechanisms of dispersion in the laminar flow through the pore space of a 3-dimensional porous medium. We focus on pre-asymptotic transport prior to the asymptotic hydrodynamic dispersion regime, in which solute motion may be described by the average flow velocity and a hydrodynamic dispersion coefficient. High performance numerical flow and transport simulations of solute breakthrough at the outlet of a sand-like porous medium evidence marked deviations from the hydrodynamic dispersion paradigm and identify two distinct regimes. The first regime is characterized by a broad distribution of advective residence times in single pores. The second regime is characterized by diffusive mass transfer into low-velocity regions in the wake of solid grains. These mechanisms are quantified systematically in the framework of a time-domain random walk for the motion of marked elements (particles) of the transported material quantity. Particle transitions occur over the length scale imprinted in the pore structure at random times given by heterogeneous advection and diffusion. Under globally advection-dominated conditions, this means Péclet numbers larger than 1, particles sample the intrapore velocities by diffusion, and the interpore velocities through advection. Thus, for a single transition, particle velocities are approximated by the mean pore velocity. In order to quantify this advection mechanism, we develop a model for the statistics of the Eulerian velocity magnitude based on Poiseuille's law for flow through a single pore, and for the distribution of mean pore velocities, both of which are linked to the distribution of pore diameters. Diffusion across streamlines through immobile zones in the wake of solid grains gives rise to exponentially distributed residence times that decay on the diffusion time over the pore length. The trapping rate is determined by the inverse diffusion time. This trapping mechanism is represented by a compound Poisson process conditioned on the advective residence time in the proposed time-domain random walk approach. The model is parameterized with the characteristics of the porous medium under consideration and captures both pre-asymptotic regimes. Macroscale transport is described by an integro-differential equation for solute concentration, whose memory kernels are given in terms of the distribution of mean pore velocities and trapping times. This approach quantifies the physical non-equilibrium caused by a broad distribution of mass transfer time scales, both advective and diffusive, on the representative elementary volume (REV). Thus, while the REV indicates the scale at which medium properties like porosity can be uniquely defined, this does not imply that transport can be characterized by hydrodynamic dispersion.

Key words: Porous Media, Dispersion, Non-Fickian Transport, Velocity Statistics, Time Domain Random Walks, Continuous Time Random Walks

† Email address for correspondence: marco.dentz@csic.es

1. Introduction

Transport of a dissolved substance or heat in the laminar flow through the void and pore space of a porous medium is due to molecular diffusion and heterogeneous advection induced by the complex pore structure. These mechanisms give rise to the asymptotic phenomenon of mechanical or hydrodynamic dispersion (Bear 1972). In order to illustrate this phenomenon, we take the view point of marked elements of the transported material quantity, or idealized solute particles, whose density is equivalent to the solute distribution, and whose motion is governed by advection and a stochastic velocity that represents diffusion (Risken 1996; Gardiner 2009). Dispersion quantifies the impact of velocity fluctuations on particle transport, similar to the concept of Brownian motion. In this context velocity fluctuations occur on a fixed characteristic time scale. Thus, particles have access to the full fluctuation spectrum at each moment, or in other words, they are statistically equal. The system is in local physical equilibrium. For transport in a porous medium, this is in general different. Velocity fluctuations occur on characteristic length scales imprinted in the porous medium structure. Particles' residence times in regions of small velocities are larger than in regions of high velocities (Saffman 1959). As a consequence, statistical equivalence between particles and thus local physical equilibrium is achieved only asymptotically for times much larger than the largest residence time.

The concept of residence times has been used in the pioneering works of de Josselin de Jong (1958) and Saffman (1959). These authors studied hydrodynamic dispersion and its mechanisms in the light of pore-scale advection and diffusion in order to determine the longitudinal (in mean flow direction) and transverse dispersion coefficients. Their approaches are based on modeling particle transport as what is now known as a time-domain or continuous time random walk (Scher & Lax 1973; Cvetkovic *et al.* 1991; Noetinger *et al.* 2016), in which particles perform transitions over a characteristic pore-length with transition times that depend on both advection and diffusion. For example, if the advection time over a pore is larger than the diffusion time, the residence time is given by the characteristic diffusion time (Saffman 1959). Bijeljic & Blunt (2006) consider pore network models characterized by broad distributions of advective residence times, which are cut-off at the diffusion time, in order to explain the dependence of longitudinal hydrodynamics dispersion coefficients on the Péclet number (Pfanckuch 1963). The Péclet number compares the diffusion to the advection time over a characteristic distance. Recent experimental and numerical works have focused on the quantification of the Péclet dependence of longitudinal and transverse hydrodynamic dispersion (Scheven 2013; Icardi *et al.* 2014).

For purely advective pore-scale transport, observed anomalous or non-Fickian transport patterns have been modeled using the continuous time random walk approach (Bijeljic *et al.* 2011, 2013; De Anna *et al.* 2013; Lester *et al.* 2014; Kang *et al.* 2014; Holzner *et al.* 2015) based on broad distributions of advective residence times. Recent numerical and experimental works, which studied purely advective particle transport through porous media, have uncovered intermittent patterns in particle velocities and accelerations as a consequence of broad distributions of flow velocities and their spatial organization (De Anna *et al.* 2013; Kang *et al.* 2014; Holzner *et al.* 2015). Other works (Siena *et al.* 2014; Gjetvaj *et al.* 2015; Jin *et al.* 2016; Matyka *et al.* 2016) have studied the distribution of flow velocities and their relation to the pore size in synthetic porous media. These works show that, in the absence of molecular diffusion, transport may be persistently anomalous, characterized by non-linear growth of the longitudinal centered mean

square displacement and tailing of the arrival time distributions of particles at a control plane. Such behaviors are caused mainly by low flow velocities as may occur close to the grains and through small pores.

As pointed out by Saffman (1959), the impact of diffusion on particle transport and transport velocities is two-fold. On one hand, it homogenises the flow velocities in single pores as particles may sample velocities across different streamlines. This is similar to particle diffusion in the flow through a circular pipe (Taylor 1953), for which the mean particle velocities asymptotically approach the mean flow velocity. On the other hand, as mentioned above, diffusion provides a cut-off mechanism if the advective transition time is much larger than the characteristic diffusion time scale over a pore. Thus, depending on the Péclet number, the time scales to reach the asymptotic regime of hydrodynamic dispersion may be very large compared to the advection time across a representative elementary volume (REV) (Bear 1972) by the average flow velocity. The REV comprises enough pore-lengths such that macroscopic medium properties as porosity and permeability, for example, can be uniquely defined. It is typically assumed that transport on the REV scale can be represented in terms of the average flow velocity and hydrodynamic dispersion coefficients (Bear 1972; Whitaker 1999; Hornung 1997), called advection-dispersion approach in the following. However, depending on the Péclet number, and on the pore-scale mass transfer mechanisms, for example between mobile and immobile porosity (Gouze *et al.* 2008; Liu & Kitanidis 2012; Gjetvaj *et al.* 2015), this may not be the case.

Current macroscale models of pore-scale transport include the advection-dispersion equation, which however, may only be valid at asymptotic times, or continuous time random walks for the modeling of purely advective non-Fickian transport. The relation between pore structure and flow velocities, and the role of advection and diffusion in preasymptotic transport remain open research questions.

We address these questions for advective-diffusive solute transport in a 3-dimensional porous medium similar in grain size distribution and porosity to sands or bead packs (Icardi *et al.* 2014), see also Figure 1. High performance computational fluid dynamics simulations of flow and transport provide the data of preasymptotic solute transport, which evidences deviations from the advection-dispersion behavior and its dependence on the Péclet number. Based on the approach of Saffman (1959), which relates the pore-diameter to the maximum pore velocity through Poiseuille’s law, we propose a link between the pore-size distribution and the distribution of the Eulerian velocity magnitudes. We then formulate particle transport as a time-domain random walk with particle transitions over a characteristic pore length and temporal transitions corresponding to the dominant advection and diffusion mechanisms. We first consider purely advective transitions, which, however, fail to describe the numerical data. We successively identify and quantify the interaction of the intra and interpore particle advection and diffusion mechanisms. These include homogenization of intrapore velocities due to diffusion across streamlines, diffusion as a transport mechanism along streamlines (Saffman 1959) and diffusion across streamlines into low velocity zones in the wake of solid grains. These mechanisms are integrated systematically into an upscaled transport model on the basis of time-domain random walks, and parameterized in terms of the statistical medium and flow properties.

The paper is organized as follows. In Section 2 the pore-scale flow and transport problem is described and the medium structure and numerical set-up are given. The simulation results for solute breakthrough curves are discussed in the light of the advection-dispersion approach. Section 3 analyses the pore-scale velocity distribution and proposes a model for the velocity magnitude and the distribution of mean pore velocities in terms of the distribution of pore-diameters. Section 4 studies the mechanisms of pore-scale

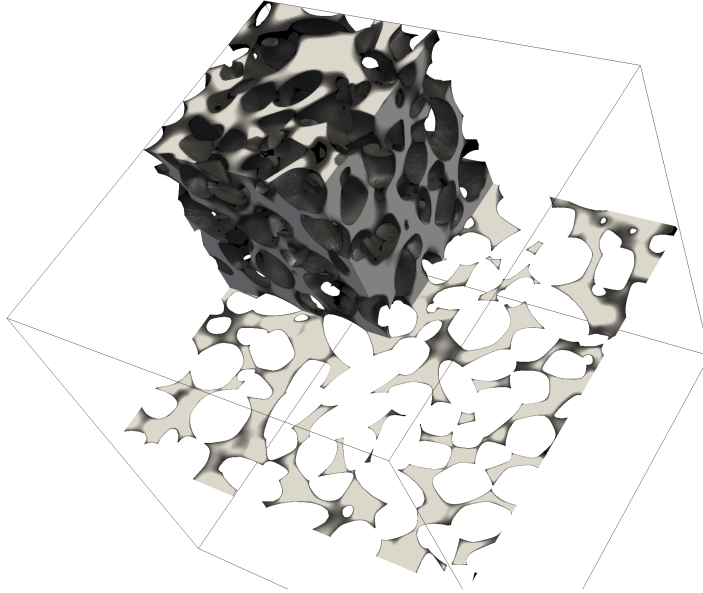


FIGURE 1. Three-dimensional (one eighth) sample of the pore space of the medium under investigation and a two-dimensional slice of it.

advection and diffusion and their impact on pre-asymptotic particle transport. These mechanisms are cast into a time-domain random walk model, which is compared against the breakthrough curves from the detailed numerical flow and transport simulations.

2. Pore Scale Flow and Transport

Flow and transport at the pore-scale are governed by the following Stokes equation for the flow velocity $\mathbf{u}(\mathbf{x})$ and the advection-diffusion equation for the conservative scalar $c(\mathbf{x}, t)$,

$$\mu \nabla^2 \mathbf{u}(\mathbf{x}) = \nabla p(\mathbf{x}) \quad (2.1)$$

$$\frac{\partial c(\mathbf{x}, t)}{\partial t} + \nabla \cdot \mathbf{u}(\mathbf{x}, t) c(\mathbf{x}, t) - D \nabla^2 c(\mathbf{x}, t) = 0, \quad (2.2)$$

where μ is viscosity, and D is the molecular diffusion coefficient. These equations are solved numerically with the open-source finite-volume code `OpenFOAM 4.x`. Details about numerical discretisation and solvers are discussed in Appendix A while boundary conditions and operating conditions are discussed below. We employ here a fully Eulerian formulation that, provided an accurate discretisation and finite diffusion coefficient, is robust and has no statistical error.

2.1. Model medium

We consider the pore-scale sample described in Icardi *et al.* (2014). As detailed in this study, the synthetic medium was generated according to the characteristics of standard sand samples. The grain size distribution was obtained from scanning electron microscopy and static-light scattering measurements and fitted by a Weibull probability density

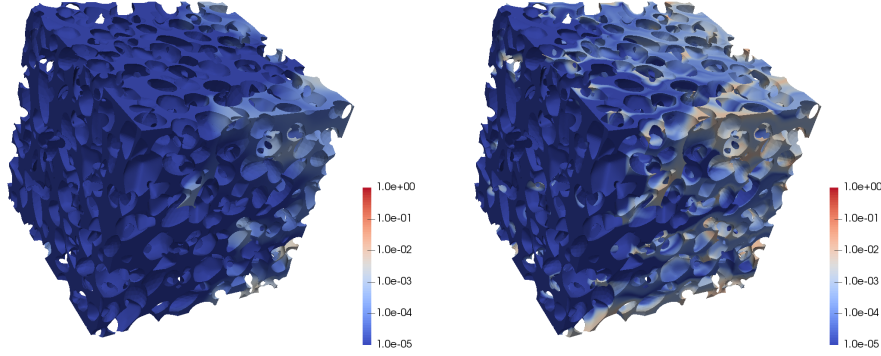


FIGURE 2. Three-dimensional snapshot of the concentration approximately $t \approx \tau_u/2$ after a pulse injection for Péclet 30 (left) and 1000 (right). Flow is from left to right.

function (PDF) for the diameter of equivalent spheres,

$$p_d(d) = \frac{k}{d_0} \left(\frac{d}{d_0} \right)^{k-1} e^{-(d/d_0)^k}. \quad (2.3)$$

The mean grain diameter is $\langle d \rangle = d_0 \Gamma(1 + 1/k) = 0.277$ mm and the Weibull parameter is $k = 7$. This distribution is sharply peaked about its mean. The synthetic porous medium was generated by sampling grain sizes from the Weibull distribution (2.3) and sedimentation of irregularly shaped grains using the software package BLENDER, which resulted in a porosity of $n = 0.35$. Note that the Weibull distribution (2.3) represents a parametric PDF to represent the empirical grain size distribution. The lognormal PDF is another frequently used parameterization for empirical grain size distributions (Friedman 1962). The model medium is cubic of length $L = 2$ mm. It contains about $2 \cdot 10^3$ grains. The characteristic pore length ℓ_0 is of the order of the mean grain size $\ell_0 \approx \langle d \rangle = 0.277$ mm. The length L of the study domain is $L = 7.22 \langle d \rangle$. The volume is of the size of a representative elementary volume in terms of the definition of volumetric porosity (Bear 1972). This means in terms of this Darcy-scale property, the medium can be considered macroscopically homogeneous. Figure 1 shows a section of the 2-dimensional porous medium and a 2-dimensional slice.

A uniform pressure boundary conditions is imposed at the inlet and the outlet, while zero-flux boundary conditions are imposed on the lateral boundaries. This results in a mean velocity $\langle \mathbf{u}(\mathbf{x}) \rangle \equiv \langle u_1 \rangle \mathbf{e}_1$ oriented towards the 1-axis of $\langle u_1 \rangle = 5.73 \cdot 10^{-6}$ m/s and identifies the characteristic advection time $\tau_u = L/\langle u_1 \rangle$. The Péclet number, which compares advective and diffusive transport over a pore length ℓ_0 , is defined by

$$Pe = \frac{\langle u_1 \rangle \ell_0}{D}. \quad (2.4)$$

2.2. Solute transport

The solute transport equation (2.2) is solved in a fully Eulerian way. Different microscopic Péclet numbers, defined by (2.4), are imposed by tuning appropriately the molecular diffusion coefficient D . Note that Pe is the only dimensionless group for the transport problem under consideration. Thus, varying the mean flow rate and varying the diffusion coefficient have the same effect as long as Pe remains unchanged. No-flux boundary

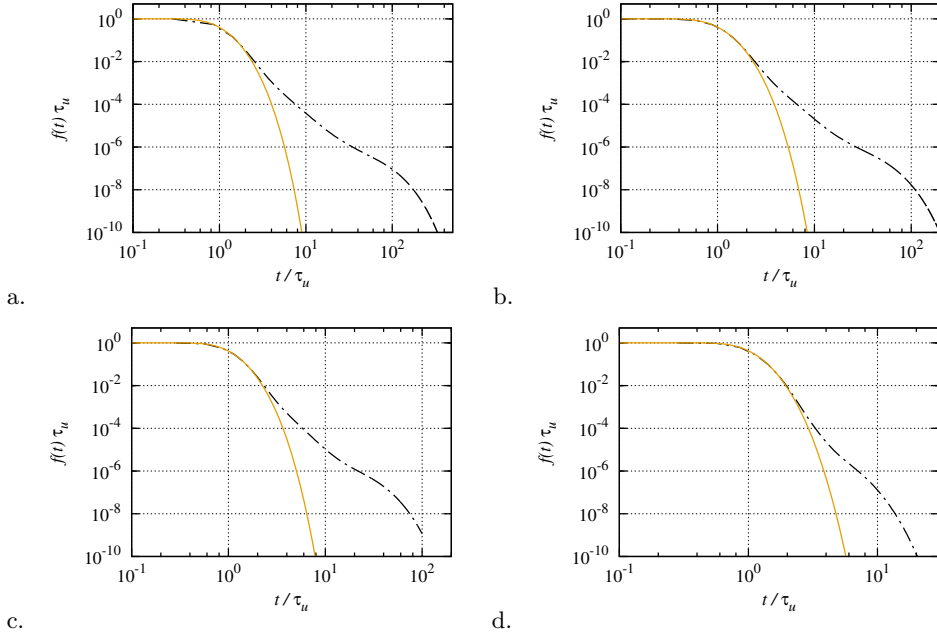


FIGURE 3. Breakthrough curves for $Pe = 10^3$, $5 \cdot 10^2$, $3 \cdot 10^2$ and 30. The dash-dotted lines in the following indicate the numerical data. The solid lines denote the solution (2.7) characterized by the dispersion coefficient \mathcal{D} which is directly fitted from the breakthrough data.

conditions are imposed at all boundaries but the inlet where a constant concentration is assumed. Figure 2 shows snapshots of the concentration distribution in the pore space. We observe increasing spatial heterogeneity with increasing Péclet number. Specifically, for the high Péclet, the invasion front is not homogeneous with regions of low solute concentration next to regions of high concentration. This is an expression of local physical non-equilibrium as discussed below.

Transport is characterized in terms of the complementary cumulative breakthrough curve defined as

$$f(t) = 1 - \frac{\int dx_2 \int dx_3 c(x_1 = L, x_2, x_3, t) u_1(x_1 = L, x_2, x_3)}{\int dx_2 \int dx_3 u_1(x_1 = L, x_2, x_3)}. \quad (2.5)$$

In the following, we refer to $f(t)$ as the breakthrough curve. Figure 3 shows the solute breakthrough curves for different Péclet number. We observe increased tailing with increasing Pe in line with the snapshots of the concentration distribution shown in Figure 2. Tailing of the breakthrough curves is an expression of local non-equilibrium because it is the result of a broad distribution of residence times in the sample.

In order to understand and interpret the breakthrough behaviour, we first consider the classical advection-dispersion approach. Icardi *et al.* (2014) quantified the cumulative complementary breakthrough curves in the light of this approach, which characterises transport in terms of an advection dispersion equation (ADE) for the evolution of the macroscale concentration $\bar{c}(x, t)$ (Whitaker 1999; Hornung 1997)

$$\frac{\partial \bar{c}(x, t)}{\partial t} + \langle u_1 \rangle \frac{\partial \bar{c}(x, t)}{\partial x} - \mathcal{D} \frac{\partial^2 \bar{c}(x, t)}{\partial x^2} = 0, \quad (2.6)$$

where \mathcal{D} is the hydrodynamic dispersion coefficient. For simplicity in the following, we denote $x = x_1$. Such a macroscale transport equation may be derived using volume averaging or homogenisation theory (Whitaker 1999; Hornung 1997). It is a valid transport description if the support scale, the representative elementary volume (Bear 1972) is well mixed. Under well-mixed conditions, the macroscale concentration $\bar{c}(x, t)$ uniquely determines the concentration on the support scale at the position x (Dentz *et al.* 2016b), which is not the case here for large Pe . The solution for the complementary cumulative breakthrough curve $f(t, x)$ at a position x in a semi-infinite medium is then given by (Kreft & Zuber 1978)

$$f(t, x) = 1 - \frac{1}{2} \left[\operatorname{erfc} \left(\frac{x-t}{\sqrt{4\mathcal{D}t}} \right) + \exp \left(\frac{x}{\mathcal{D}} \right) \operatorname{erfc} \left(\frac{x+t}{\sqrt{4\mathcal{D}t}} \right) \right]. \quad (2.7)$$

The latter is a good approximation to the solution for a finite domain for $Pe \gg 1$, which is fulfilled for the scenarios of interest here. We denote $f(t) = f(t, x = L)$. Figure 3 compares (2.7) to the numerical data for different Pe . The onset and initial decay of the breakthrough curve are well represented by the mean flow velocity and a fitted dispersion coefficient \mathcal{D} . However, it fails to capture the tailing behaviour at intermediate and long times. This implies that the system is not at local equilibrium, the support scale is not well-mixed. In the following we analyse these transport features and their origins in terms of spatial fluctuations of the pore-scale flow velocity and the effect of molecular diffusion. The aim is to gain understanding of the pore-scale transport mechanisms in order to arrive at a macroscale transport approach that can be quantified in terms of the pore-scale velocity, pore size distributions and molecular diffusion. We first discuss the statistical properties of the Eulerian velocity and velocity magnitude in the light of the pore-size distribution before we analyze the mechanisms of pore-scale transport and their macroscale quantification in terms of $f(t)$.

3. Eulerian Velocity Distributions and Pore Scale Velocity Model

In order to understand the pore-scale dispersion behaviour, we study here the Eulerian velocity distribution and its interpretation in terms of the grain and pore-size distribution. We consider the distribution of the velocity components in mean flow direction, $u_1(\mathbf{x})$, and perpendicular to it, $u_i(\mathbf{x})$ for $i \neq 1$, as well as the velocity magnitude $v_e(\mathbf{x}) = \sqrt{\sum_i u_i(\mathbf{x})^2}$. The Eulerian velocity PDFs are computed as volume weighted histograms over the entire pore-space ω

$$p_e(v) = \frac{1}{V_\omega} \int_{\omega} d\mathbf{x} \delta[v - v(\mathbf{x})], \quad (3.1)$$

where V_ω is the pore volume; $v(\mathbf{x}) = u_i(\mathbf{x})$ for the PDF of velocity components and $v(\mathbf{x}) = v_e(\mathbf{x})$ for the PDF of the velocity magnitude. Note that these PDFs generally depend on the sampling volume. For the sand-like porous medium under consideration here, the sampling volume is of the size of an REV, thus the velocity PDF is assumed not to change significantly when increasing the sampling volume.

The PDFs of the velocity components are shown in Fig. 4. The distributions of the components perpendicular to the mean flow direction are symmetric around 0 and have an exponential shape. The PDF of the longitudinal component is skewed towards positive values with an approximately stretched exponential shape (Siena *et al.* 2014; Holzner *et al.* 2015). It is non-zero for small negative velocities, which indicates the presence of

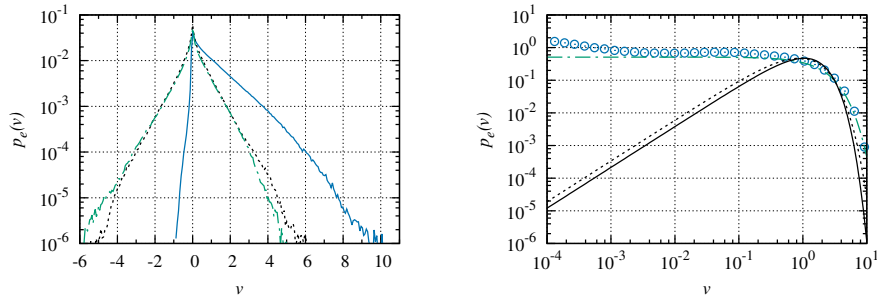


FIGURE 4. (Left) PDF of (solid) $u_1(\mathbf{x})$ (dashed) $u_2(\mathbf{x})$ and (dash-dotted) $u_3(\mathbf{x})$. (Right) (circles) PDF of the magnitude of Eulerian velocities and (dash-dotted) estimation with the velocity model (3.10) for $v_0 = 2.1\langle u_1 \rangle$ and $\alpha = 2.5$. The solid line denotes the PDF (3.14) of mean pore velocities, the dashed line its approximation by (3.16). Velocities are normalized by $\langle u_1 \rangle$.

back-flow. It is not clear how to relate the distributions of the velocity components to statistical characteristics of the porous medium.

In order to relate the medium properties to the Eulerian flow field, we focus rather on the PDF of velocity magnitudes illustrated in Figure 4. The PDF is flat from 10^{-3} to 1, from which on it decays exponentially fast. As detailed below, the flat distribution at small velocities can be understood by sampling a parabolic velocity profile, the smooth cut-off at larger velocities may be related to the distribution of pore-sizes. The deviation from the flat profile at small velocities may be attributed to low velocity zones in the wake of solid grains as discussed in Section 4.2.

First, we consider the mean of the Eulerian velocity magnitude. It is related to the mean velocity through the advective tortuosity χ as (Koponen *et al.* 1996)

$$\langle v_e \rangle = \chi \langle u_1 \rangle. \quad (3.2)$$

The advective tortuosity measures the ratio of average trajectory length to linear distance. For the model medium under consideration, the mean flow velocity is $\langle u_1 \rangle = 5.7 \cdot 10^{-6}$ m/s, and the mean velocity magnitude $\langle v_e \rangle = 9 \cdot 10^{-6}$ m/s. Thus, the tortuosity is given by $\chi = \langle v_e \rangle / \langle u_1 \rangle = 1.6$.

In the following, we study the PDF of velocity magnitudes based on the assumption that the velocity profile in a single pore is parabolic (Saffman 1959; Lester *et al.* 2013; Holzner *et al.* 2015; De Anna *et al.* 2017). The validity of this assumption is underlined qualitatively by the velocity profiles shown in Fig. 5, which are obtained along a cut of the three-dimensional porous medium of Fig. 2. Note that some authors (Le Borgne *et al.* 2011) have studied flow and transport in wavy tubes, this means a serial arrangement of pores, as a model system for the upscaling of pore-scale heterogeneity. This view is not appropriate for more complex porous media, for which the network aspect is important in the sense that pore intersections exist such that the concept of the linear pore breaks down. Some aspect of flow in serial and parallel pore arrangements are discussed in (Holzner *et al.* 2015).

The PDF (3.1) of the velocity magnitude can be decomposed into the contributions from the individual pores as

$$p_e(v) = \sum_p \frac{V_p}{V_\omega} \frac{1}{V_p} \int_{\omega_p} d\mathbf{x} \delta[v - v(\mathbf{x})], \quad (3.3)$$

where ω_p is the single pore domain and V_p its volume. The velocity $v(\mathbf{x}) \equiv v(r)$ depends

only on the pore radius and is given by

$$v(r) = v_p \left[1 - \left(\frac{2r}{a_p} \right)^2 \right], \quad (3.4)$$

where a_p is the pore diameter and r is the distance from the pore axis. The maximum velocity v_p in a pore is given by $v_p = v_0(a_p/a_0)^2$ with v_0 a characteristic velocity and a_0 a characteristic pore diameter. Under this assumption, we obtain

$$p_e(v) = \sum_p \frac{V_p}{V_\omega} \frac{1}{v_p} H(v_p - v), \quad (3.5)$$

where $H(v)$ denotes the Heaviside step function. Note that the velocity PDF in a single pore is uniform between 0 and the maximum velocity v_p , which can be seen by sampling $v(r)$ given by (3.4) uniformly in a pore cross-section.

We furthermore assume that the pore volume is $V_p = ba_p^2\ell_p$ with b a shape factor, ℓ_p the pore length and a_p the pore diameter. In the following, we assume that the pore length $\ell_p \approx \ell_0$ is approximately constant, while the pore diameter a_p is variable. For the sand-like medium under consideration, the pore-length is of the order of the grain size. As the grain size distribution (2.3) is sharply peaked, we approximate it as constant. The pore diameter in contrast depends on the distance of the grains in the packing, which is much more variable. This is indicated in the two-dimensional slice of the porous medium shown in Figure 1. We can now write

$$p_e(v) = \sum_p \frac{ba_0^2\ell_0}{V_\omega} \frac{1}{v_0} H[v_0(a_p/a_0)^2 - v]. \quad (3.6)$$

This expression can be written tautologically as

$$p_e(v) = \int da \frac{ba_0^2\ell_0 N_0}{V_\omega} \frac{1}{v_0} H[v_0(a/a_0)^2 - v] \left[\frac{1}{N_0} \sum_p \delta(a - a_p) \right], \quad (3.7)$$

where N_0 is the number of pores. We note that the expression in square brackets on the right side is equal to the PDF of pore diameters $p_a(a)$, and define the average volume of a single pore as $\langle V_p \rangle = V_\omega/N_0$. Thus, expression (3.7) can be written as

$$p_e(v) = \int da \frac{ba_0^2\ell_0}{\langle V_p \rangle} \frac{1}{v_0} H[v_0(a/a_0)^2 - v] p_a(a), \quad (3.8)$$

The grain size distribution is given by a Weibull distribution. We assume for the pore-size distribution also a Weibull distribution with

$$p_a(a) = \frac{\alpha}{a_0} \left(\frac{a}{a_0} \right)^{\alpha-1} \exp[-(a/a_0)^\alpha]. \quad (3.9)$$

We note that the average pore volume is $\langle V_p \rangle \propto a_0^2\ell_0$. Using these relations in (3.8), we obtain after integration and normalisation the following estimation for the Eulerian velocity PDF,

$$p_e(v) = \frac{\exp[-(v/v_0)^{\alpha/2}]}{v_0\Gamma(1 + 2/\alpha)}. \quad (3.10)$$

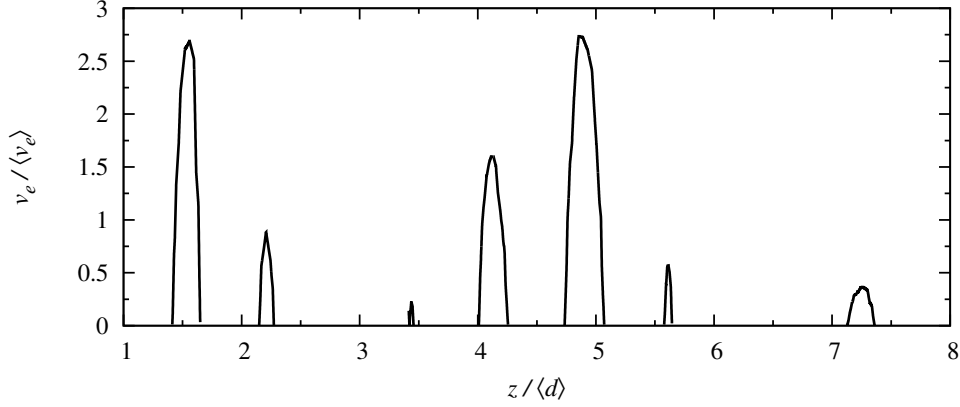


FIGURE 5. Velocity profile across the porous medium perpendicular to the main flow direction.

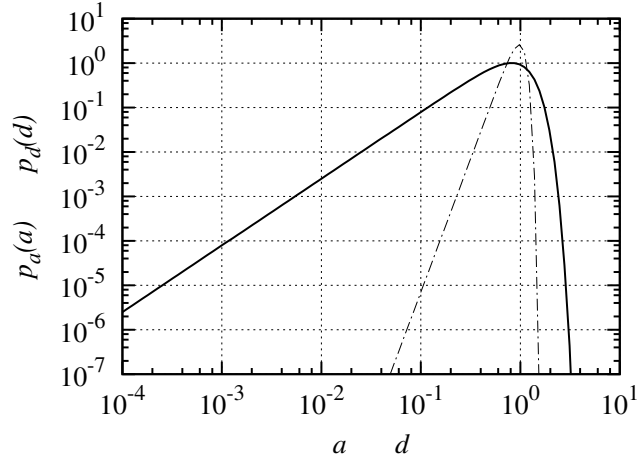


FIGURE 6. The dash-dotted line illustrates the PDF of grain diameters (2.3) for $d_0 = 1$, the solid line shows the corresponding PDF of pore diameters (3.9) for $a_0 = 1$ obtained from the proposed velocity model.

The mean velocity is given by

$$\langle v_e \rangle = v_0 \frac{\Gamma(4/\alpha)}{\Gamma(2/\alpha)}. \quad (3.11)$$

By fitting the Eulerian velocity data, we estimate an exponent of $\alpha \approx 2.5$ and $v_0 \approx 2.1\langle u_1 \rangle$, which has the same average velocity of $\langle v_e \rangle = 1.6\langle u_1 \rangle$ as the data. The proposed velocity model implies that the PDF of pore diameters can be characterized by a Weibull distribution with $\alpha = 2.5$. Figure 6 shows the grain size PDF $p_d(d)$ of grain diameters and the PDF of pore diameters $p_a(a)$ estimated from the above velocity model. The distribution of pore diameters is much more variable than the grain size distribution, specifically toward low values. This is intuitive because the pore size is related to the distance between grains in the packings, which can be much smaller than the grain size, see also Figure 1.

From the PDF of pore diameters, we can estimate the PDF of mean velocities $v_m =$

$v_p/2$, which is

$$p_m(v) = \int da \frac{ba^2 \ell_0}{\langle V_p \rangle} \delta[v_0(a/a_0)^2/2 - v] p_a(a), \quad (3.12)$$

By setting again $\langle V_p \rangle \propto a_0^2 \ell_0$ and using the Weibull distribution (3.9), we obtain

$$p_m(v) \propto \frac{1}{v_0} \int da \delta(a^2 - 2v/v_0) \alpha a^{\alpha+1} \exp[-a^\alpha]. \quad (3.13)$$

Evaluating the Dirac delta and normalising gives

$$p_m(v) = \frac{\alpha}{v_0 \Gamma(1 + 2/\alpha)} \left(\frac{2v}{v_0} \right)^{\frac{\alpha}{2}} \exp \left[- \left(\frac{2v}{v_0} \right)^{\alpha/2} \right]. \quad (3.14)$$

We thus obtain for the average of v_m

$$\langle v_m \rangle = v_0 \frac{\Gamma(1 + 4/\alpha)}{2\Gamma(1 + 2/\alpha)} = v_0 \frac{\Gamma(4/\alpha)}{\Gamma(2/\alpha)} \equiv \langle v_e \rangle \quad (3.15)$$

Expression (3.14) implies that $p_m(v) \propto v^{a-1}$ with $a = \alpha/2 + 1$. The PDF of the mean velocities is characterised by lower weights than the Eulerian PDF on both low and high velocities. This is illustrated in Figure 4. We approximate (3.14) in the following by the Γ -distribution

$$p_m(v) = \frac{1}{v_\gamma \Gamma(a)} \left(\frac{v}{v_\gamma} \right)^{a-1} \exp \left(- \frac{v}{v_\gamma} \right), \quad (3.16)$$

where $a = \alpha/2 + 1$ and $v_\gamma = \langle v_e \rangle / a$. The quality of this approximation is shown in Figure 4. As we will see in the following, the PDF of mean velocities plays an important role for the interpretation of solute dispersion under finite Péclet numbers.

4. Pore-Scale Transport Mechanisms and Upscaling

We study the pore scale transport mechanisms in the light of heterogeneous advection and diffusion in the pore space. As discussed above, pore scale transport mechanisms have been characterised by advection-dispersion models in terms of the average pore velocity $\langle u_1 \rangle$ and effective dispersion coefficients \mathcal{D} (e.g. Icardi *et al.* 2014; Scheven *et al.* 2007; Bijeljic *et al.* 2004), and dual domain models (Liu & Kitanidis 2012; Gjetvaj *et al.* 2015) to capture the impact of diffusion into the immobile porosity and low velocity regions. The impact of advective heterogeneity has been studied in the framework of continuous time and time domain random walks (Bijeljic & Blunt 2006; Le Borgne *et al.* 2011; Bijeljic *et al.* 2011; De Anna *et al.* 2013; Kang *et al.* 2014; Gjetvaj *et al.* 2015; Holzner *et al.* 2015). Here we analyse in detail the interplay of heterogeneous advection from the intra to the inter-pore scale and diffusion in order to identify and quantify the dominant transport mechanisms.

To this end, we model solute transport in a particle-based framework through spatial transitions over the characteristic pore length $\ell \sim \ell_0$ with a (variable) duration τ (Saffman 1959). In this picture, the position x_n and time t_n of a solute particle along the mean flow direction are given after n steps as

$$x_{n+1} = x_n + \xi_n, \quad t_{n+1} = t_n + \tau_n. \quad (4.1)$$

The spatial step ξ_n may be downstream or upstream depending on the local advection and diffusion conditions. The transition length is given by $|\xi_n| = \ell/\chi$. Particles make

transitions along their trajectory of length ℓ . The random walk (4.1), however, describes transport along the mean flow direction. Thus, the transition length is corrected by the advective tortuosity χ , which accounts for the fact that particle trajectories through the pore space are not straight. The transition time τ_n depends on the pore-scale advection and diffusion mechanisms as discussed in detail below, and illustrated schematically in Figure 7. We assume that the advection and diffusion properties at subsequent positions are statistically independent, which implies that the τ_n are identical independent random variables. This is a reasonable assumption because flow and particle velocities are only weakly correlated between pores (Saffman 1959; Le Borgne *et al.* 2011; Bijeljic *et al.* 2011; De Anna *et al.* 2013; Lester *et al.* 2013; Kang *et al.* 2014; Holzner *et al.* 2015).

Equation (4.1) describes a time-domain random walk (TDRW) (Cvetkovic *et al.* 1991; Delay *et al.* 2005; Painter & Cvetkovic 2005; Russian *et al.* 2016; Noetinger *et al.* 2016), or equivalently a continuous time random walk (CTRW) (Montroll & Weiss 1965; Scher & Lax 1973; Berkowitz *et al.* 2006). It is characterised by the joint PDF of transition length ξ and time τ denoted by $\psi(x, t)$, which encodes the pore-scale transport mechanisms. The marginal PDF of transition times is defined by

$$\psi(t) = \int dx \psi(x, t). \quad (4.2)$$

The evolution of the macroscale solute concentration in this framework is given by the generalised Master equation (Kenkre *et al.* 1973; Berkowitz *et al.* 2006; Comoli *et al.* 2016)

$$\frac{\partial \bar{c}(x, t)}{\partial t} = \int dx' \int_0^t dt' \mathcal{K}(x - x', t - t') [\bar{c}(x', t') - \bar{c}(x, t')]. \quad (4.3)$$

It expresses the fact that the change of solute concentration at a given position depends on the transport history and in this sense accounts for incomplete mixing, or non-uniqueness of concentration on the support scale. The macroscale concentration at a given position is composed of solute particles with different transport histories, which is quantified by the distribution of transition times. The memory kernel $\mathcal{K}(x, t)$ denotes the probability per time of a particle transition of length $x - x'$ during time $t - t'$. It relates solute fluxes at earlier times $t' < t$ to concentration changes at time t . Under Markovian conditions, the change of the solute concentration is only determined by the local in time solute fluxes. The memory kernel is given in terms of the distribution of transition length and times. It is defined through its Laplace transform as

$$\mathcal{K}^*(x, \lambda) = \frac{\lambda \psi^*(x, \lambda)}{1 - \psi^*(\lambda)}. \quad (4.4)$$

The Laplace transform is defined in Abramowitz & Stegun (1972), Laplace transformed quantities are marked by an asterisk, the Laplace variable is denoted by λ . If the kernel $\mathcal{K}(\mathbf{x}, t)$ is short-range in x , this means it decays sufficiently fast for $|x|$ larger than a characteristic length scale, (4.3) can be localised in space (Berkowitz *et al.* 2002; Dentz *et al.* 2004),

$$\frac{\partial \bar{c}(x, t)}{\partial t} + \int_0^t dt' \left[\nu(t - t') \frac{\partial \bar{c}(x, t')}{\partial x} - \kappa(t - t') \frac{\partial^2 \bar{c}(x, t')}{\partial x^2} \right] = 0. \quad (4.5)$$

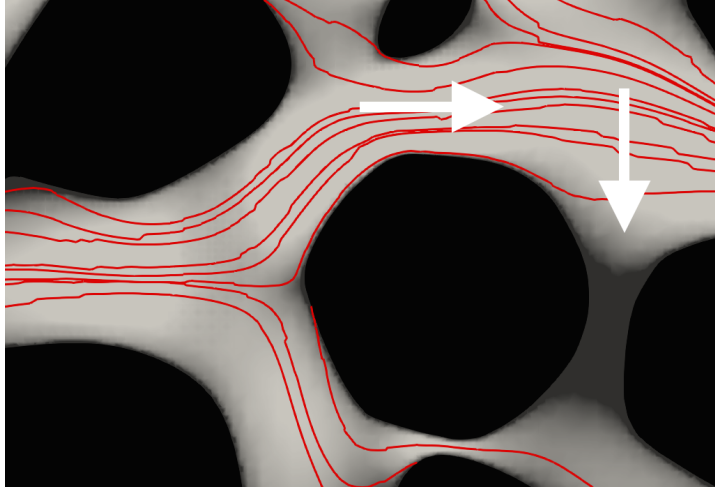


FIGURE 7. Schematic of transitions in the time-domain random walk model (4.1). The thin red lines represent streamlines of the flow in a cross-section of the porous medium. The shading of the background denotes the absolute value of the flow velocity, which decreases from light to dark, black areas denote the grains. The horizontal arrow denotes particle transitions over the length of a pore in streamwise direction, the vertical arrow indicates particle transitions across streamlines into low velocity zones in the wake of the solid grains. Transitions along streamlines are due to mean advection in the pore and diffusion. Transitions across the streamlines are due to diffusion. Particles that enter the immobile zones remain there for the residence time τ_f before they are released back into the mobile portion of the medium.

The drift and diffusion kernels are defined by

$$\nu(t) = \int dx x \mathcal{K}(x, t) \quad (4.6a)$$

$$\kappa(t) = \frac{1}{2} \int dx x^2 \mathcal{K}(x, t). \quad (4.6b)$$

In the following, we solve for the macroscale transport behaviour using random walk particle tracking simulations based on (4.1). The solute arrival time at a position x is thus given by (Comolli *et al.* 2016)

$$\tau_a(x) = t_{n_a(x)}, \quad n_a(x) = \inf(n | x_n \geq x), \quad (4.7)$$

where $n_a(x)$ is the number of steps a particle requires to arrive at the outlet. The distribution of arrival times, denoted by $p_a(t, x)$ is defined by

$$p_a(t, x) = \langle \delta[t - \tau_a(x)] \rangle. \quad (4.8)$$

The complementary cumulative breakthrough curve, or in the following only breakthrough curve, is thus given by

$$f(t, x) = \int_t^\infty dt' p_a(t', x) = \langle H[\tau_a(x) - t] \rangle, \quad (4.9)$$

where $H(t)$ is the Heaviside step function. Expression (4.9) is the probability that the arrival time is larger than t . In the following, we denote the breakthrough curve at the outlet at $x = L$ by $f(t) \equiv f(t, x = L)$.

Equation (4.1) for the particle motion and its counterpart (4.3) for the particle distri-

bution describe the non-local evolution of macroscale concentration due to local physical non-equilibrium, but are not predictive as long as $\psi(x, t)$ is not known. However, the TDRW approach provides a framework to identify and quantify the dominant pore-scale transport mechanisms in terms of the distribution of the Eulerian flow velocity and the diffusion properties in the medium. Thus, in the following we investigate the structure of $\psi(x, t)$ in the light of the dominant pore-scale transport mechanisms and their manifestations on large scale transport.

Figure 7 show a schematic of possible particle transitions. Solute particles move along the pores due to advection-diffusion and may access low velocity regions in the wake of the grains by diffusion only. We first consider the impact of heterogeneous advection and diffusion along streamlines on the behaviour of the arrival time distribution. Then we study the influence of diffusion across streamlines into low velocity zones and its quantification. Finally, we consider the combined impact of advective heterogeneity and diffusion along and across pores on large scale transport.

4.1. Heterogeneous advection and diffusion

We analyse here the role of heterogeneous advection and diffusion along the streamlines within and between pores. To this end, we first consider purely advective particle motion and the resulting large scale transport behaviour in terms of the particle arrival time distributions. Then, we analyse the effect of diffusion first on the intra-pore and then on the inter-pore particle motion.

4.1.1. Pure advection

For infinite Pe , this means, purely advective transport, (4.1) becomes

$$x_{n+1} = x_n + \frac{\ell}{\chi}, \quad t_{n+1} = t_n + \frac{\ell}{v_n} \quad (4.10)$$

Particles move only forward along streamlines and the transition times $\tau_n = \ell/v_n$ denote the advection time over the distance ℓ by the velocity magnitude v_n . The magnitudes v_n of particle velocities are distributed according to the stream-wise velocity PDF $p_s(v)$ defined as follows. First we note that the TDRW (4.1) samples particle velocities equidistantly along trajectories, while the Eulerian velocity PDF is sampled volumetrically in space. For divergence-free flow, $p_s(v)$ is related to the Eulerian velocity PDF through flux weighting (Saffman 1959; Dentz *et al.* 2016a; Comolli & Dentz 2017)

$$p_s(v) = \frac{vp_e(v)}{\langle v_e \rangle}. \quad (4.11)$$

This relation can be understood qualitatively by noting that low flow velocities occupy wider streamtubes than high velocities because of fluid volume conservation. Thus, volumetric sampling emphasises low flow velocities. Equidistant velocity sampling along streamlines on the other hand, weighs high and low velocities equally. This difference in sampling between the Eulerian and streamwise velocity distributions is compensated in (4.11) through flux weighting.

With this relation, the PDF of purely advective transition times denoted here by $\psi_a(t)$ can be directly related to the distribution $\psi_a(t)$ of advective transition times as

$$\psi_a(t) = \frac{\ell}{t^3 \langle v_e \rangle} p_e(\ell/t). \quad (4.12)$$

The Eulerian PDF $p_e(v)$ goes towards a constant at small velocities and is cut-off as a stretched exponential at large velocities, see Figure 4 and (3.10). For the numerical

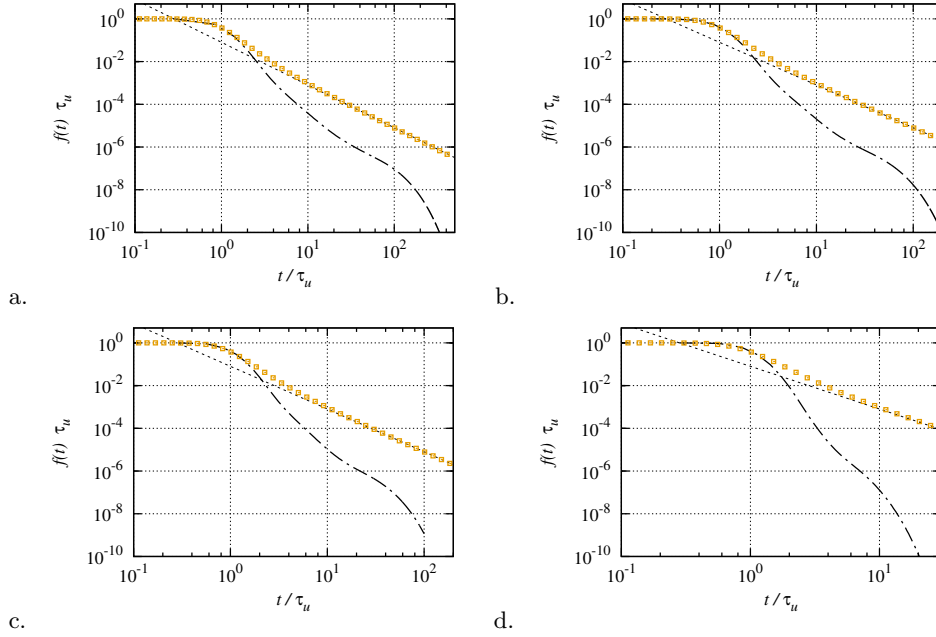


FIGURE 8. Breakthrough curves for $Pe = 10^3$, $5 \cdot 10^2$, $3 \cdot 10^2$, and 30. The symbols denote the breakthrough curves obtained from the TDRW (4.10) based on purely advective transport, $Pe = \infty$, for the transition length $\ell \approx 0.84\ell_p$. The dashed lines show the predicted t^{-2} -scaling. The TDRW simulations use 10^9 particles.

implementation of the TDRW, we approximate the Eulerian velocity PDF (3.10) by an exponential distribution characterised by the same mean velocity. Specifically, the characteristic that determines the late time behaviour of the breakthrough curve is the behaviour of $p_e(v)$ at small velocities $v \ll \langle v_e \rangle$, for which it is constant. Thus, from (4.12), we obtain that the PDF of transition times behaves as $\psi_a(t) \propto t^{-1-b}$ with $b = 2$ for times $t \gg \tau_u$. Thus, $\psi_a(t)$ is an asymptotically stable distribution.

The breakthrough, or arrival times at the outlet are given by

$$\tau_a = \sum_{i=1}^{n_a} \tau_i, \quad (4.13)$$

where the number of steps $n_a = \lceil L\chi/\ell \rceil$, where $\lceil \cdot \rceil$ is the ceiling function. As $\psi_a(t)$ is stable, the PDF of arrival times, as a sum of stable random variables, has the same long time behaviour as $p_f(t, x) \propto t^{-1-b}$. Thus, the breakthrough curve is $f(t, x) \propto t^{-b}$, see (4.9). This means here that the breakthrough curve is predicted to behave as $f(t) \propto t^{-2}$. Figure 8 compares the numerically obtained breakthrough curves for different Péclet numbers to the predictions of (4.10) parameterised by the advective transition time PDF (4.12). The purely advective breakthrough curve is of course independent of Pe and shows the t^{-2} -decay as predicted. Also here, the onset and initial decay of the breakthrough curves are well captured, but the purely advective model fails to represent the tails of the pore-scale data. It overestimates the tailing, while the ADE model underestimates it.

For all Pe , we observe two distinct tailing behaviours. An intermediate tail whose decay is slower than the exponential tail predicted by the ADE, and a flatter long-time tail that is cut-off exponentially. The slope of the intermediate tail and the onset and final

decay of the late-time tail clearly depend on the Péclet number and thus on diffusion. In the following, we study these mechanisms in more detail.

4.1.2. Advection under diffusion

Diffusion acts on how particles experience the flow velocities in two ways. Firstly, within a pore diffusion enables particles to sample the flow profile across the pore (Saffman 1959; Haber & Mauri 1988; Dentz & Carrera 2007). This implies that the effective velocity experienced by a particle along a pore tends toward the mean velocity v_m . The velocity extremes are attenuated by diffusion. It is these extremes, particularly the low velocities close to the pore walls, which cause the t^{-2} -tails predicted by the purely advective model. If the diffusion time across the pore is smaller than the characteristic advection time along the pore, particles move effectively with the mean velocity v_m (Saffman 1959). This is a good approximation here because the estimated distribution of pore diameters is much broader than the distribution of pore lengths, and tailed towards small values as shown in Figure 6. This means that the transport relevant velocity distribution is the PDF of mean pore velocities (3.14) rather than the PDF (3.10) of point-wise velocities. Note that the mean pore velocities are still sampled volumetrically, while the particle velocities are sampled spatially along streamlines. Thus, as outlined above, the distribution of particle velocities is given by flux-weighting of $p_m(v)$ as

$$p_s(v) = \frac{vp_m(v)}{\langle v_e \rangle}. \quad (4.14)$$

Recall that $\langle v_m \rangle = \langle v_e \rangle$.

Secondly, the transition time over the pore length is the result of advection by the mean pore velocity and diffusion. For example, for pores whose advection time ℓ/v_m is larger than the diffusion time $\ell^2/2D$ along the pore, the particle transition time is dominated by diffusion. The transition time is limited by the characteristic diffusion time (Saffman 1959). The distribution of advective-diffusive transit times over a given distance can be seen as a first passage problem (Redner 2001) characterised by v_m and the diffusion coefficient D . Here, these mechanisms are captured by quantifying the transition time as an exponentially distributed random variable whose mean is given in terms of the harmonic mean between the advection and the diffusion times over the length ℓ (Delay *et al.* 2005; Noetinger *et al.* 2016; Russian *et al.* 2016)

$$\psi_0(t|v) = \frac{\exp(-t/\tau_v)}{\tau_v}, \quad \tau_v = \frac{\ell/v}{1 + \frac{2D}{v\ell}} \quad (4.15)$$

The latter is an approximation for the true first-passage time PDF and can be derived from a finite volume discretisation of the advection-diffusion equation (Russian *et al.* 2016). Furthermore, depending on the relative strength of diffusion and advection within the pore, particles may move up or downstream. The probability $w_u(v)$ for an upstream transition is given by (Russian *et al.* 2016)

$$w_u(v) = \frac{D\tau_v}{\ell^2} \quad (4.16)$$

and for downstream motion correspondingly $w_d(v) = 1 - w_u(v)$. Thus, the PDF $\Lambda(x|v)$ of transition length for a given velocity v reads as

$$\Lambda(x|v) = [w_d(v)\delta(x - \ell/\chi) + w_u(v)\delta(x + \ell/\chi)]. \quad (4.17)$$

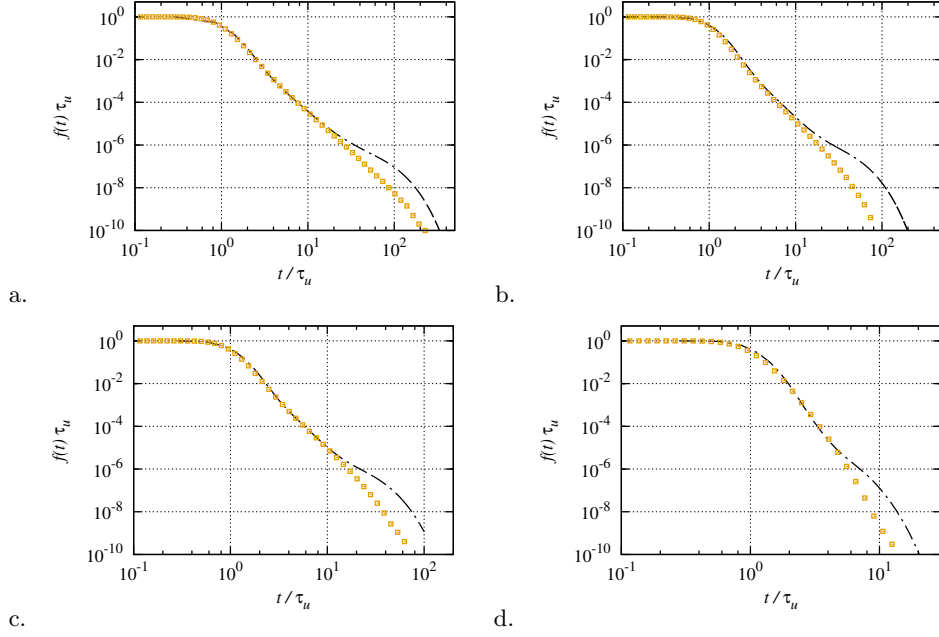


FIGURE 9. Breakthrough curves for $Pe = 10^3$, $3 \cdot 10^2$, 30 and 3. The dash-dotted lines indicate the numerical data, the symbols the TDRW model for $\ell \approx \ell_p$ for $Pe = 10^3$, $\ell = 0.77\ell_p$ for $Pe = 5 \cdot 10^2$, and $Pe = 3 \cdot 10^2$ and $\ell = 0.7\ell_p$ for $Pe = 30$.

The global joint PDF of transition lengths and times then is given by

$$\psi_m(x, t) = \int_0^\infty dv \frac{vp_m(v)}{\langle v_e \rangle} \Lambda(x|v) \psi_0(t|v). \quad (4.18)$$

The transition time PDF is obtained by marginalisation according to (4.2),

$$\psi_m(t) = \int_0^\infty dv \frac{vp_m(v)}{\langle v_e \rangle} \psi_0(t|v). \quad (4.19)$$

Using these expressions, we obtain for the drift and diffusion kernels (4.6a) and (4.6b) the following Laplace space expressions,

$$\nu_m^*(\lambda) = \int_0^\infty dv \frac{v^2 p_m(v)}{\chi \langle v_e \rangle} \frac{1 - \psi_0^*(\lambda|v)}{1 - \psi_m^*(\lambda)} \quad (4.20a)$$

$$\kappa_m^*(\lambda) = \int_0^\infty dv \frac{(D + v\ell/2)vp_m(v)}{\chi^2 \langle v_e \rangle} \frac{1 - \psi_0^*(\lambda|v)}{1 - \psi_m^*(\lambda)}, \quad (4.20b)$$

see Appendix B.

We solve this TDRW model for the breakthrough curves using random walk particle tracking simulations. Figure 9 shows the results of this TDRW characterized by (4.18) compared to the direct numerical simulations of the pore scale flow and transport problem. Note that the TDRW is parameterized by the PDF of mean pore velocities and the Péclet number. For computational convenience, here and in the following, we ap-

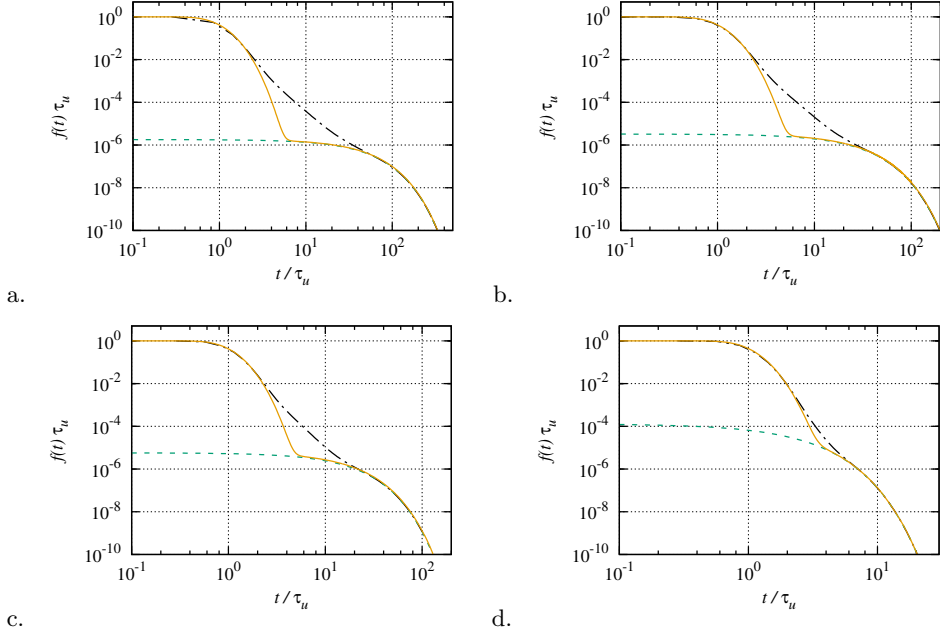


FIGURE 10. Breakthrough curves for $Pe = 10^3$, $3 \cdot 10^2$, 30 and 3. The dash-dotted lines indicate the numerical data, the circles indicate the exponential estimation of the tailing behaviour, from which we obtain the values for $\langle \tau_f \rangle$ and γ displayed in Figure 11 below.

proximate the PDF (3.14) of mean pore velocities by (3.16). The TDRW model captures correctly the intermediate tailing of the breakthrough curves at all Péclet numbers, which thus can be attributed to both heterogeneity in the mean pore velocity and diffusion.

Note that the PDF of transition times (4.19) is not heavy tailed. The maximum transition time is given by $\ell^2/2D$, which determines the cut-off of (4.19). For smaller times, it behaves as $\psi_m(t) \propto t^{-3-\alpha/2}$, which can be seen by inserting (3.14) into (4.19) and rescaling of the integration variable. Thus, according to the central limit theorem, breakthrough curves at large distances from the inlet are expected to converge to a Fickian limit. In this sense, the tailing behavior in the intermediate regime is pre-asymptotic and can be attributed to the distance from the inlet or sample size. At times longer than the characteristic diffusion time over the pore, the TDRW breakthrough curves are cut-off and do not capture the second tailing regime characterized by first a flattening and then exponential cut-off. In the following, we discuss the origin of the second tailing regime in the light of trapping due to particle transitions across streamlines into low-velocity pores.

4.2. Solute trapping and release

In the previous section, we have focused on particle motion in direction of the streamlines by the mean pore velocity as illustrated schematically by the horizontal arrow in Figure 7. Alternatively, particles may make diffusive transitions across streamlines into the wake of a solid grain, indicated by the vertical arrow in Figure 7. In these regions, the flow velocity is close to zero and diffusion is the dominant transport mechanisms. Thus, we denote these regions in the following as immobile zones.

We first focus solely on the impact of cross-diffusion into low velocity zones and represent heterogeneity of the pore velocities in terms of the average velocity $\langle v_e \rangle$ and the

hydrodynamic dispersion coefficients \mathcal{D} determined above. This means that we assume that advective heterogeneity can be homogenised by advection-dispersion. Below in Section 4.3, we combine the effects of heterogeneous advection and diffusion into immobile zones. As we assume that mobile transport is homogenised, there is no characteristic transition length scale in contrast to the previous sections, where the pore-length ℓ marks the correlation scale of the stream-wise velocities. Velocity fluctuations are quantified by hydrodynamic dispersion. Thus, in terms of the advective-diffusive TDRW introduced in the previous section, this means that particles perform spatial transitions over a distance $\Delta s \ll L$, which now merely represents a discretisation of space (Russian *et al.* 2016). Particle transitions in space then are characterized by (4.16) and (4.17) with the substitutions

$$\ell \rightarrow \Delta s, \quad v \rightarrow \langle v_e \rangle, \quad D \rightarrow \mathcal{D}. \quad (4.21)$$

Particle transitions in time now are composed of a mobile time τ_0 , which represents advective-dispersive motion in mean flow direction and the time of trapping in immobile zones as $\tau = \tau_0 + \tau_{im}(\tau_0)$. The mobile time is distributed according to (4.15) with the substitutions (4.21). The immobile time τ_{im} is determined based on the assumption that immobile zones are uniformly distributed in the medium. As the characteristic time scale between trapping events is given by the characteristic cross-diffusion time, trapping events can be assumed to occur at a constant rate γ . This means that the number of trapping events n_{τ_0} that occur during a time τ_0 are Poisson-distributed,

$$p_n(n|\tau_0) = \frac{(\gamma\tau_0)^n \exp(-\gamma\tau_0)}{n!}, \quad (4.22)$$

Thus, the immobile time τ_{im} during a mobile transition of duration τ_0 is given by the sum over the n_{τ_0} individual trapping times times τ_f ,

$$\tau_{im}(\tau_0) = \sum_{k=1}^{n_{\tau_0}} \tau_{f,k}. \quad (4.23)$$

It is a compound Poisson process (Feller 1968). The trapping times τ_f are independent identically distributed according to $p_f(t)$, which is determined below. The compound Poisson process (4.23) is characterized by the PDF $\psi_f(t|\tau_0)$, whose Laplace transform is given by (Margolin *et al.* 2003)

$$\psi_f^*(\lambda|\tau_0) = \exp\left(-\left\{\lambda + \gamma\left[1 - p_f^*(\lambda)\right]\right\}\tau_0\right). \quad (4.24)$$

In order to quantify the impact of cross-diffusion on macroscale transport, we need to determine the distribution of trapping times τ_f and the trapping rate γ . To this end, we first note that the total concentration can be decomposed into the concentration $c_m(x, t)$ of the solute in the mobile and $c_{im}(x, t)$ in the immobile regions, $\bar{c}(x, t) = c_m(x, t) + c_{im}(x, t)$. Note that here both mobile and immobile concentrations refer to the same support volume. The mobile concentration in this TDRW framework is described by the non-local advection-diffusion equation (Margolin *et al.* 2003; Benson & Meerschaert 2009; Russian *et al.* 2016; Comolli *et al.* 2016)

$$\frac{\partial c_m(x, t)}{\partial t} + \langle u_1 \rangle \frac{\partial c_m(x, t)}{\partial x} - \mathcal{D} \frac{\partial^2 c_m(x, t)}{\partial x^2} = -\frac{\partial c_{im}(x, t)}{\partial t}. \quad (4.25)$$

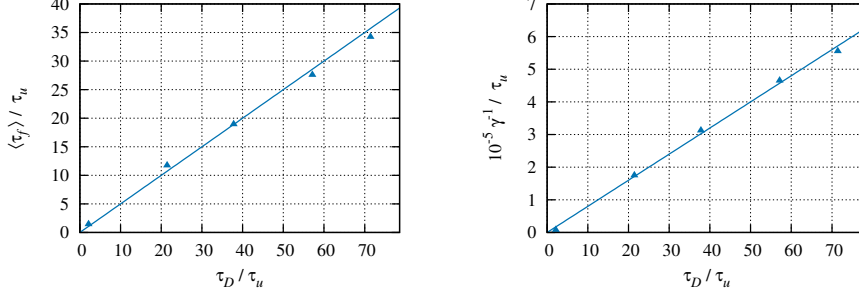


FIGURE 11. (Left panel) Mean trapping time $\langle \tau_f \rangle$ versus τ_D estimated from the data and (solid line) linear estimation with $r = 1/2$. (Right panel) Inverse trapping rate versus τ_D and linear estimate with $\beta = 2.5 \cdot 10^{-4}$.

The immobile concentration $c_{im}(x, t)$ is given by

$$c_{im}(x, t) = \int_0^t dt' \left[\int_{t-t'}^{\infty} dt'' p_f(t'') \right] \gamma c_m(x, t'). \quad (4.26)$$

The expression in the square brackets denotes the probability that the trapping time is larger than $t - t'$. This means, the immobile concentration is given by the probability per time that a particle enters in the immobile zone expressed by $\gamma c_m(x, t)$ times the probability that it stays there for a time larger than the observation time. The ratio β of total mass in the immobile and mobile zones at equilibrium is obtained from (4.26) as

$$\beta = \gamma \langle \tau_f \rangle. \quad (4.27)$$

Note that (4.25) describes solute transport in the multirate mass transfer approach (Haggerty & Gorelick 1995; Carrera *et al.* 1998; Comolli *et al.* 2016). In this framework, β is equal to the ratio between the immobile ϕ_{im} and mobile volume fraction ϕ_m . Thus, the trapping rate is given by

$$\gamma = \frac{\phi_{im}}{\phi_m \langle \tau_f \rangle}, \quad (4.28)$$

Using the mobile and immobile volume fractions, the total concentration $\bar{c}(x, t)$ can be written in terms of $g_m(x, t) = c_m(x, t)/\phi_m$ and $g_{im}(x, t) = c_{im}(x, t)$, which refer to the mobile and immobile subvolumes, as $\bar{c}(x, t) = \phi_m g_m(x, t) + \phi_{im} g_{im}(x, t)$.

From (4.25), we obtain for the long-time behaviour of the breakthrough curves the following behaviour,

$$f(t) = \tau_u \gamma \int_t^{\infty} dt' p_f(t'). \quad (4.29)$$

for $t \gg \tau_u$. The full solution for $f(t)$ and the derivation of this approximation are detailed in Appendix D. This means, the tailing behaviour is fully determined in terms of the PDF of trapping times. Figure 10 shows that the tail of the breakthrough curve can well be approximated by an exponential function, which implies that the distribution of trapping times can be represented by an exponential PDF. In fact, the distribution of diffusion times in an immobile zone of size ℓ can be obtained through the solution of a diffusion problem as outlined in Appendix D. The average trapping time is related to the

characteristic diffusion time $\tau_D = \ell^2/(2D)$ in a domain of length ℓ . The PDF of trapping times for such a problem is well approximated again by the exponential distribution as (Delay *et al.* 2002; Dentz *et al.* 2012).

$$p_f(t) = \frac{\exp(-t/\langle\tau_f\rangle)}{\langle\tau_f\rangle}, \quad (4.30)$$

see also Appendix E. The mean trapping time is $\langle\tau_f\rangle = r\tau_D$ with $r \sim 1$. The tail of the breakthrough curve is thus given by

$$f(t) = \tau_u \gamma \exp(-t/r\tau_D). \quad (4.31)$$

This means, we can obtain both the trapping rate and the mean trapping time from the tails of the breakthrough curves at different Péclet numbers. According to our reasoning, both depend on τ_D as

$$\langle\tau_f\rangle = r\tau_D, \quad \gamma = \frac{\beta}{r\tau_D}, \quad (4.32)$$

The dependences of $\langle\tau_f\rangle$ and γ^{-1} on τ_D estimated from the numerical data are shown in Figure 11. From the data, we obtain $r \approx 1/2$ and $\beta \approx 2.5 \cdot 10^{-4}$, which is consistent with the probability of obtaining velocities smaller than $10^{-3}\langle v \rangle$, which we deem immobile. Note from Figure 4 that the PDF of the velocity magnitude deviates from the flat behaviour characteristic for in-pore velocities at 10^{-3} and increases towards lower velocities. This increase may be assigned to low velocities in immobile zones.

Figure 10 compares the breakthrough curves obtained from the solution of (4.25) (see Appendix D) parameterized with an exponential PDF of trapping times and the average trapping times and trapping rates given by (4.32) as well as the mean velocity $\langle u_1 \rangle$ and hydrodynamic dispersion coefficient \mathcal{D} . It captures well the onset of decay of the breakthrough curves just like the ADE solution discussed above, and the exponential long-time tail. The onset of the exponential tail depends on the trapping rate γ , the exponential cut-off time is given by the diffusion time scale τ_D . As expected, this TDRW model does not represent the intermediate tailing due to heterogeneous pore velocities. The quantification of the combined effect of trapping and heterogeneous advection is discussed in the next section.

4.3. Advective Heterogeneity and Trapping

In this section, we integrate heterogeneous pore-scale advection, and diffusion into immobile zones into a TDRW approach that quantifies the dominant pore-scale transport mechanisms. This approach models mobile particle transition over the length of a pore as detailed in Section 4.1.2. Solute trapping is modelled as discussed in the previous section. Specifically, the number of trapping event is given by the Poisson distribution (4.22) conditioned on the time $\tau_m = \ell/v$ for a mobile transition. Thus, the transition time in this integrated TDRW is (Russian *et al.* 2016; Comolli *et al.* 2016)

$$\tau = \tau_m + \sum_{k=1}^{n_{\tau_m}} \tau_{f,k}, \quad (4.33)$$

where n_{τ_m} is distributed according to the Poisson distribution $p_n(n|\tau_m)$ and τ_f according to (4.30). Note that the total trapping time during a mobile transition given by the second term on the right side of (4.33) is a compound Poisson process. The joint PDF $\psi(x, t)$ of transition lengths ξ and time τ can then be expressed in Laplace space in terms of the Laplace transforms of $\psi_m(t)$, the PDF of mobile times, and the trapping time PDF $p_f(t)$

as

$$\psi^*(x, \lambda) = \psi_m^*(x, \lambda + \gamma[1 - p_f^*(\lambda)]), \quad (4.34)$$

see Appendix C. The distribution of transition times is given accordingly by

$$\psi^*(\lambda) = \psi_m^*(\lambda + \gamma[1 - p_f^*(\lambda)]). \quad (4.35)$$

With these results, we obtain for the velocity and diffusion kernels (4.6a) and (4.6b) the Laplace space expressions

$$\nu^*(\lambda) = \frac{\nu_m[\lambda\Phi^*(\lambda)]}{\Phi^*(\lambda)} \quad (4.36a)$$

$$\kappa^*(\lambda) = \frac{\kappa_m[\lambda\Phi^*(\lambda)]}{\Phi^*(\lambda)}. \quad (4.36b)$$

where $\Phi^*(\lambda) = 1 + \lambda^{-1}\gamma[1 - p_f^*(\lambda)]$, see Appendix B. Following the developments in the previous section, we define the immobile concentration $c_{im}(x, t)$ in terms of the mobile concentration as in (4.26). Thus, based on this relation and expressions (4.36) for the kernels, we derive from (4.5) the following governing equation for the solute concentration in the mobile regions,

$$\begin{aligned} \frac{\partial c_m(x, t)}{\partial t} + \frac{\partial}{\partial t} \int_0^t dt' \left[\int_{t-t'}^{\infty} dt'' p_f(t'') \right] \gamma c_m(x, t') = \\ - \int_0^t dt' \int_0^{t-t'} dt'' \left[\nu_m(t'') \frac{\partial}{\partial x} - \kappa_m(t'') \frac{\partial^2}{\partial x^2} \right] \psi_f(t-t'-t''|t'') c_m(x, t'), \end{aligned} \quad (4.37)$$

see Appendix F. The second term on the left side denotes the change of the mobile solute concentration due to mass transfer with the immobile regions. The term on the right side denotes the solute flux in the mobile region during the period of time t'' for which particles are making mobile transitions. Note that $\psi_f(t-t'-t''|t'')$ denotes the probability that the particle is trapped during the time $t-t'-t''$ for a given mobile duration t'' .

We solve this TDRW model for macroscale transport using random walk particle tracking simulations. The transport behaviour is parameterized in terms of the PDF of mean pore-velocities, and the trapping rate γ , (4.28), and the distribution (4.30) of trapping times discussed in the previous section. Thus, in principle, macroscale transport can be understood in terms of the medium geometry (distribution of pore diameters), hydrodynamics (Poiseuille's law), and diffusion along and across streamlines into immobile regions.

Figure 4.3 compares the breakthrough curves from the direct numerical simulations to the behaviour of the TDRW approach. The TDRW model and simulation data compare well for all Péclet numbers. The intermediate tailing is well captured by the distribution of mean pore-velocities and diffusion in mean flow direction as discussed in Section 4.1.2. The exponential tail is picked up by the mass transfer model discussed in the previous section. Also, the transitions from the intermediate advective tailing behaviour to the exponential are well represented for all Péclet number. The proposed model captures all aspects of the observed solute breakthrough curves based on the identification and quantification of the dominant pore-scale transport mechanisms.

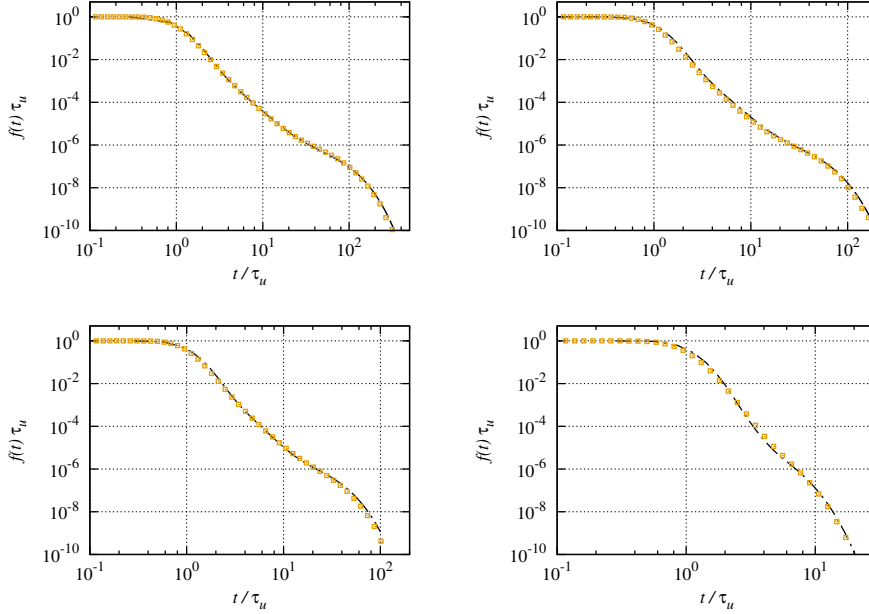


FIGURE 12. Breakthrough curves for $Pe = 10^3$, $5 \cdot 10^2$, $3 \cdot 10^2$ and 30. The dash-dotted line indicate the numerical results. The symbols denote the result of the TDRW model including heterogeneous advection and trapping in immobile zones. The TDRW model uses the parameter values given in the captions of Figures 9 and 10.

5. Summary and Conclusions

We have studied and quantified the advection and diffusion mechanisms of preasymptotic pore-scale transport and their relations to the statistical medium and flow properties in terms of the pore size distribution and the distribution of the magnitude of the Eulerian velocity. Our study uses data from high performance computational fluid dynamics simulations of flow and solute transport in a synthetic 3-dimensional porous medium. The medium properties resemble the characteristics of sand or bead packs in grain size distribution and porosity.

We focus on the complementary solute breakthrough curves at the outlet of the porous medium, to which we refer as breakthrough curve for simplicity. The advection-dispersion paradigm predicts an exponential decrease of the breakthrough curve from 1 towards 0 at the mean advection time over the domain length with a width given in terms of the longitudinal hydrodynamic dispersion coefficient. For all $Pe \gg 1$ we observe pronounced deviations from this behaviour, which increase with increasing Pe . The breakthrough curves display two non-Fickian regimes. The intermediate regime is given by a sub-exponential decay, which can be attributed to advective heterogeneity. The second, regime is characterised by a flattening of the sub-exponential behavior before it is cut-off exponentially fast. This behaviour can be attributed to diffusion across streamlines into the immobile regions in the wake of solid grains.

In order to quantify these behaviors in a macroscale transport model, we first develop a model for the statistics of the Eulerian velocity magnitude in terms of the pore-size distribution. This model relies on the assumption that the velocity profile in a single pore is parabolic and that its maximum velocity is related to the cross-sectional pore area through Poiseuille's law. Thus, we obtain an estimate for the distribution of point-wise

velocity magnitudes as well as an estimate for the distribution of mean pore velocities. The distribution of velocity magnitudes is characterized by a flat part at small velocities, which can be attributed to the flat distribution characteristic for velocities in single pores, and an exponential decay that can be attributed to the pore-size distribution. The distribution of mean pore velocities is much narrower than the distribution of the Eulerian velocity magnitude, with smooth cut-offs at low and high velocity magnitudes.

Then, we cast the advective-diffusive pore-scale particle motion in terms of a time-domain random walk (TDRW), based on the fact that flow velocities vary little over the characteristic pore length. We first consider purely advective particle transitions such that the distribution of residence times is given in terms of the distribution of the Eulerian velocity magnitude. It scales as t^{-3} , which implies a Levy-stable behavior for the particle travel time distributions, and predicts a Pe -independent, persistent t^{-2} -scaling of the breakthrough curves. This approach ignores completely the impact of diffusion on pore-scale particle transport. Thus, in a next step, we account for the diffusive sampling of flow velocities in single pores. Based on the assumption that pores are in average much longer than wide, we approximate the effective particle velocity over a pore by the average pore velocity. This assumes that particles can sample the full pore velocity contrast during a transition. Thus, the distribution of effective particle velocities is set equal to the distribution of mean pore-velocities. We also account for the diffusive cut-off of the residence time distribution in case of diffusion-dominated transitions. The resulting TDRW captures the intermediate tailing of the breakthrough curves and the dependence on the Péclet number despite these drastic simplifications. The flattening of the breakthrough curve and asymptotic exponential cut-off is not accounted for. As mentioned above, this feature can be attributed to purely diffusive particle transitions across streamlines into the void space in the wake of solid grains that connect adjacent pores. This mechanism represents a trapping process, whose residence times can be characterized by an exponential distribution which decays on the diffusion time over a pore. The trapping rate can be related to the volume fractions of mobile and immobile pore regions and the inverse diffusion time. Trapping of particles is quantified in the TDRW framework by a compound Poisson process conditioned on the advective residence time. This approach captures the full behavior of the breakthrough curves for all Pe . The evolution of the particle density, or equivalently solute distribution, is governed by an integro-partial differential equation, whose memory kernels are related to the distribution of mean pore velocities and the distribution of residence times in immobile pores. Note that we have focused on global transport in the direction of the mean flow. The presented approach can be generalised to account for transverse mass transfer by determining the stochastic rules of transverse particle motion, which here is quantified in an average sense through tortuosity.

In conclusion, we have identified and quantified the dominant pore-scale advection and diffusion mechanism in a macroscale transport model that captures pre-asymptotic non-Fickian transport. This approach accounts for the impact of pore-scale heterogeneity on transport on the REV scale, which manifests in tailing of the breakthrough curves as an expression of pore-scale concentration heterogeneity. Thus, while the concept of the REV is valid for the definition of macroscale material properties such as porosity or permeability, it does not imply that transport is in local physical equilibrium. The occurrence of advective breakthrough curve tailing in the intermediate regime depends on the distance from the inlet and the distribution of characteristic advection time scales, while the non-Fickian asymptotic tail due to trapping in immobile zones depends on the characteristic diffusion time in the immobile regions. We suggest that the identified transport mechanism are of a general nature beyond the sand-like model medium under

consideration here. More complex porous media are characterized by broad distribution of pore diameters and immobile porosity (Gouze *et al.* 2008; Bijeljic *et al.* 2013; Gjetvaj *et al.* 2015), which emphasise the non-Fickian pre-asymptotic transport features and may delay the onset of an asymptotic hydrodynamic dispersion regime.

MD and JJH gratefully acknowledge the support of the European Research Council (ERC) through the project MHetScale (617511) and the support of the Spanish Ministry of Economy, Industry and Competitiveness through the project MECMAT (CGL2016-80022-R). MI gratefully acknowledges the financial support provided by AVL and the computing facilities provided by the Warwick Centre for Scientific Computing.

Appendix A. Numerical simulations

The standard OpenFOAM solvers `simpleFoam` and `scalarTransportFoam` have been used to perform, respectively, flow and transport simulations. The latter has been modified to allow for runtime co-processing of volumetric and PDF information.

A blended forward Euler/Crank-Nicolson discretisation in time has been used that ensures $\Delta t < \Delta x^2/D$ for accurate time resolution. A second-order upwind scheme is used for advection to minimize numerical dispersion, a second-order least square approach is used for computing gradients and a central scheme for diffusive fluxes.

The simulations are performed on an irregular grid to represent well the grain boundaries. Details on the mesh-generation and numerical method are given in Icardi *et al.* (2014). In Sections III and IV of this paper, the interested reader finds a detailed grid independence study of the flow and transport simulations. The number of mesh cells used for the numerical solution is $41 \cdot 10^6$. The largest cell size is $\ell_c = 1/200$, the smallest $\ell_c/1600$ of the domain size. Simulations were performed on 128 Intel Xeon E5-2630 2.4GHz cores and, due to the significant tailing, have to be run for long times, resulting in approximately 48h of simulation time per each run.

Regarding the issue of numerical dispersion, for the numerical simulations used in the manuscript, the maximum grid Péclet number $Pe_g = \ell_c v/D$ varies between $Pe_g \approx 5$ for the $Pe = 10^3$ case and $Pe_g \approx 0.15$ for the $Pe = 30$ case. Note that these are the maximum grid Peclet numbers, which are obtained in the pore centers, where the resolution is coarsest and velocities are relatively high, of the order of the mean velocity. As both the mesh-size and velocity vary, the grid Peclet numbers close to grains and in the wake of the grains, where the resolutions are high (i.e., small ℓ_c) and velocities are low, the grid Peclet numbers are $Pe_g \ll 1$. Also, note that for the breakthrough curves under consideration (e.g., Figure 3), the effect of hydrodynamic dispersion due to flow variability (in high flow velocities), which is of the order of $\bar{v}\ell_0$, overshadows the possible effect of numerical dispersion in the pore centers, which would otherwise only be visible in the initial decay of the breakthrough curve. The tailings in the two intermediate regimes are caused by variability in low velocities (high velocities give rise to the hydrodynamic dispersion effect) and dominant diffusion in immobile zones, for which the local grid Péclet numbers are much smaller than 1. For this reason, we are confident that the numerical simulations accurately reflect the actual physical mass transfer processes in the porous medium.

Appendix B. Kernels

We derive here expressions (4.20) and (4.36). To this end, we consider the i th moments of the Laplace transform of the $\psi(x, t)$

$$\mu_i^*(\lambda) = \int dx x^i \psi^*(x, \lambda). \quad (\text{B } 1)$$

The Laplace transforms of the kernels (4.6) are then given in terms of the $\mu_i^*(\lambda)$ as

$$\nu^*(\lambda) = \frac{\mu_1^*(\lambda)}{1 - \psi^*(\lambda)} \quad (\text{B } 2a)$$

$$\kappa^*(\lambda) = \frac{1}{2} \frac{\mu_2^*(\lambda)}{1 - \psi^*(\lambda)}. \quad (\text{B } 2b)$$

We obtain by using the Laplace transform of (4.18)

$$\mu_{1,m}^*(\lambda) = \frac{\ell}{\chi} \int_0^\infty dv \frac{v^2 \tau_v p_m(v)}{\langle v_e \rangle} \frac{\lambda \psi_0^*(\lambda|v)}{1 - \psi_0^*(\lambda|v)} [1 - \psi_0^*(\lambda|v)] \quad (\text{B } 3)$$

$$\mu_{2,m}^*(\lambda) = \int_0^\infty dv \frac{2D + v\ell}{\chi^2} \frac{v \tau_v p_m(v)}{\langle v_e \rangle} \frac{\lambda \psi_0^*(\lambda|v)}{1 - \psi_0^*(\lambda|v)} [1 - \psi_0^*(\lambda|v)] \quad (\text{B } 4)$$

Inserting the Laplace transform of the exponential $\psi_0(t|v)$ then gives

$$\mu_{1,m}^*(\lambda) = \frac{\ell}{\chi} \int_0^\infty dv \frac{v^2 p_m(v)}{\langle v_e \rangle} [1 - \psi_0^*(\lambda|v)] \quad (\text{B } 5)$$

$$\mu_{2,m}^*(\lambda) = \int_0^\infty dv \frac{2D + v\ell}{\chi^2} \frac{v p_m(v)}{\langle v_e \rangle} [1 - \psi_0^*(\lambda|v)]. \quad (\text{B } 6)$$

Inserting these expressions into (B 2) gives (4.20).

Similarly, we obtain by using (4.34) in (B 2)

$$\mu_1^*(\lambda) = \frac{\ell}{\chi} \int_0^\infty dv \frac{v^2 \tau_v p_m(v)}{\langle v_e \rangle} \frac{\lambda \Phi^*(\lambda) \psi_0^*[\lambda \Phi^*(\lambda)|v]}{1 - \psi_0^*[\lambda \Phi^*(\lambda)|v]} \frac{1 - \psi_0^*[\lambda \Phi^*(\lambda)|v]}{\Phi^*(\lambda)} \quad (\text{B } 7)$$

$$\mu_2^*(\lambda) = \int_0^\infty dv \frac{2D + v\ell}{\chi^2} \frac{v \tau_v p_m(v)}{\langle v_e \rangle} \frac{\lambda \Phi^*(\lambda) \psi_0^*[\lambda \Phi^*(\lambda)|v]}{1 - \psi_0^*[\lambda \Phi^*(\lambda)|v]} \frac{1 - \psi_0^*[\lambda \Phi^*(\lambda)|v]}{\Phi^*(\lambda)}, \quad (\text{B } 8)$$

where we defined $\Phi^*(\lambda) = 1 + \lambda^{-1} \gamma [1 - p_f^*(\lambda)]$. Inserting the Laplace transform of the exponential $\psi_0(t|v)$ then gives

$$\mu_1^*(\lambda) = \frac{\ell}{\chi} \int_0^\infty dv \frac{v^2 p_m(v)}{\langle v_e \rangle} \frac{1 - \psi_0^*[\lambda \Phi^*(\lambda)|v]}{\Phi^*(\lambda)} \quad (\text{B } 9)$$

$$\mu_2^*(\lambda) = \int_0^\infty dv \frac{2D + v\ell}{\chi^2} \frac{v p_m(v)}{\langle v_e \rangle} \frac{1 - \psi_0^*[\lambda \Phi^*(\lambda)|v]}{\Phi^*(\lambda)}. \quad (\text{B } 10)$$

By comparison with (B 5) and (B 6), we observe that

$$\mu_1^*(\lambda) = \frac{\mu_{1,m}^*[\lambda\Phi^*(\lambda)]}{\Phi^*(\lambda)} \quad (\text{B 11})$$

$$\mu_2^*(\lambda) = \frac{\mu_{2,m}^*[\lambda\Phi^*(\lambda)]}{\Phi^*(\lambda)}. \quad (\text{B 12})$$

Inserting these expressions into (B 2) gives (4.36).

Appendix C. Transition time distribution

Here we derive expression (4.34) for the Laplace transform of the transition time PDF for the case of heterogeneous advection and trapping. The trapping time, the second term in (4.33) is a compound Poisson process, whose distribution is $\psi_f(t|\tau_m)$, see (4.24). Thus, for a given τ_m , the Laplace transform of the joint PDF of transition length and time is

$$\psi^*(\lambda|\tau_m) = \exp\left(-\left\{\lambda + \gamma[1 - p_f^*(\lambda)]\right\}\tau_m - \lambda\tau_m\right). \quad (\text{C 1})$$

For a given v , then the distribution of transition times is obtained by averaging of (C 1),

$$\begin{aligned} \psi^*(\lambda|v) &= \int_0^\infty dt \exp\left(-\left\{\lambda + \gamma[1 - p_f^*(\lambda)]\right\}t - \lambda t\right) \psi_0(t|v) \\ &= \psi_0^*(\lambda + \gamma[1 - p_f^*(\lambda)]). \end{aligned} \quad (\text{C 2})$$

The joint PDF of transition length and time is thus

$$\psi^*(\lambda) = \int_0^\infty dv \frac{vp_m(v)}{\langle v_e \rangle} \psi_0^*(\lambda + \gamma[1 - p_f^*(\lambda)]) = \psi_m^*(\lambda + \gamma[1 - p_f^*(\lambda)]). \quad (\text{C 3})$$

Appendix D. Breakthrough curves

We determine here the solution for the breakthrough curve corresponding to the governing equation (4.25). As at the beginning of Section 4 for the ADE-model, we consider a semi-infinite domain, which is a good approximation for $Pe \gg 1$, which is the case for all the scenarios under consideration here. Furthermore, we notice that Laplace transform of (4.25) is given by

$$\lambda c_m^*(x, \lambda) + \langle u_1 \rangle \frac{\partial c_m^*(x, \lambda)}{\partial x} - \mathcal{D} \frac{\partial^2 c_m^*(x, \lambda)}{\partial x^2} = 0, \quad (\text{D 1})$$

where we used (4.26) and the fact that the initial concentration is 0. Furthermore, we defined

$$\varphi^*(\lambda) = \lambda^{-1} [1 - p_f^*(\lambda)]. \quad (\text{D 2})$$

Note that (D 1) is identical in form to the Laplace transform of (2.6). Thus, the solution can be expressed in terms of the Laplace transform of (2.7) as (Dentz *et al.* 2004)

$$f^*(\lambda, x) = \frac{1}{\lambda} - \frac{1}{\lambda} \exp\left[-\frac{x\langle u_1 \rangle}{2\mathcal{D}} \left(\sqrt{1 + 4\frac{\lambda\mathcal{D}[1 + \gamma\varphi^*(\lambda)]}{\langle u_1 \rangle^2}}\right) - 1\right]. \quad (\text{D 3})$$

The solutions of (4.25) for the breakthrough curves displayed in Figure 10 are obtained by numerical inverse Laplace transform of (D 3). In the limit $\lambda D / \langle u_1 \rangle^2 \ll 1$, we can expand the latter as

$$f^*(\lambda, x) = \frac{x[1 + \gamma\varphi^*(\lambda)]}{\langle u_1 \rangle} + \dots, \quad (\text{D 4})$$

where the dots denote subleading contributions. Thus, we obtain for $f(t, L) \equiv f(t)$ the long-time approximation (4.29).

Appendix E. Trapping time distribution

In order to make an estimate for the distribution of trapping time, we approximate diffusion into immobile pores as a 1-dimensional first passage problem. Particles are injected at $z = 0$ and diffuse to the outlet at $z = \ell$. The particle distribution $g(z, t)$ then follows the diffusion equation

$$\frac{\partial g(z, t)}{\partial t} - D \frac{\partial^2 g(z, t)}{\partial z^2} = 0 \quad (\text{E 1})$$

for the boundary conditions

$$-D \frac{\partial g(z=0, t)}{\partial z} = \delta(t), \quad g(z = \ell, t) = 0, \quad (\text{E 2})$$

and the initial condition $g(z, t=0) = 0$. The distribution of first passage times at $z = \ell$ is given by the flux over the boundary as

$$p_f(t) = -D \frac{g(z = \ell, t)}{\partial z}. \quad (\text{E 3})$$

The solution to (E 1) reads in Laplace space as

$$g^*(z, \lambda) = \frac{\sinh \left[\sqrt{\frac{\lambda}{D}} (\ell - z) \right]}{\sqrt{\lambda D} \cosh \left(\sqrt{2\lambda\tau_D} \right)}. \quad (\text{E 4})$$

Using the latter in the Laplace transform of (E 3) gives

$$p_f^*(\lambda) = \frac{1}{\cosh \left(\sqrt{2\lambda\tau_D} \right)}. \quad (\text{E 5})$$

For $\lambda\tau_D \ll 1$ (E 5) can be approximated by

$$p_f^*(\lambda) \approx \frac{1}{1 + \lambda\tau_D}, \quad (\text{E 6})$$

whose inverse Laplace transform is given by (4.30).

Appendix F. Governing equation under heterogeneous advection and trapping

In order to derive (4.37), we note that the governing equation for the Laplace transform $\bar{c}^*(x, \lambda)$ follows from (4.5) and (4.36) as

$$\lambda \bar{c}^*(x, \lambda) + \left(\nu_m^* [\lambda \Phi^*(\lambda)] \frac{\partial}{\partial x} - \kappa_m^* [\lambda \Phi^*(\lambda)] \frac{\partial^2}{\partial x^2} \right) \frac{\bar{c}^*(x, \lambda)}{\Phi^*(\lambda)} = c(x, t=0). \quad (\text{F 1})$$

The Laplace transform of the immobile concentration (4.26) is given by

$$c_{im}^*(x, \lambda) = \gamma \lambda^{-1} \left[1 - p_f^*(\lambda) \right] c_m^*(x, \lambda), \quad (\text{F } 2)$$

such that the total concentration is $\bar{c}^*(x, \lambda) = \Phi^*(\lambda) c_m^*(x, \lambda)$. Thus, (F 1) can be written in terms of the mobile concentration $c_m^*(x, \lambda)$ as

$$\lambda \Phi^*(\lambda) c_m^*(x, \lambda) + \left(\nu_m^* [\lambda \Phi^*(\lambda)] \frac{\partial}{\partial x} - \kappa_m^* [\lambda \Phi^*(\lambda)] \frac{\partial^2}{\partial x^2} \right) c_m^*(x, \lambda) = c(x, t = 0). \quad (\text{F } 3)$$

Its inverse Laplace transform gives (4.37).

REFERENCES

- ABRAMOWITZ, M & STEGUN, I. A. 1972 *Handbook of Mathematical Functions*. Dover Publications, New York.
- BEAR, J. 1972 *Dynamics of fluids in porous media*. American Elsevier, New York.
- BENSON, D. A. & MEERSCHAERT, M. M. 2009 A simple and efficient random walk solution of multi-rate mobile/immobile mass transport equations. *Adv. Wat. Res.* **32** (4), 532–539.
- BERKOWITZ, B., CORTIS, A., DENTZ, M & SCHER, H. 2006 Modeling non-fickian transport in geological formations as a continuous time random walk. *Rev. Geophys.* **44**, RG2003.
- BERKOWITZ, B., KLAFTER, J., METZLER, R. & SCHER, H. 2002 Physical pictures of transport in heterogeneous media: Advection-dispersion, random-walk, and fractional derivative formulations. *Water Resour. Res.* **38** (10), 1191.
- BIJELJIC, B. & BLUNT, M. J. 2006 Pore-scale modeling and continuous time random walk analysis of dispersion in porous media. *Water Resour. Res.* **42**, W01202.
- BIJELJIC, BRANKO, MOSTAGHIMI, PEYMAN & BLUNT, MARTIN J 2011 Signature of non-fickian solute transport in complex heterogeneous porous media. *Phys. Rev. Lett.* **107** (20), 204502.
- BIJELJIC, B., MUGGERIDGE, A. H. & BLUNT, M. J. 2004 Pore-scale modeling of longitudinal dispersion. *Water Resour. Res.* **40**, W11501.
- BIJELJIC, B., RAEINI, A., MOSTAGHIMI, P. & J., BLUNT M. 2013 Predictions of non-fickian solute transport in different classes of porous media using direct simulation on pore-scale images. *Phys. Rev. E* **87**, 013011.
- CARRERA, J., SÁNCHEZ-VILA, X., BENET, I., MEDINA, A., GALARZA, G. & GUIMERÀ, J. 1998 On matrix diffusion: formulations, solution methods, and qualitative effects. *Hydrogeology Journal* **6**, 178–190.
- COMOLLI, A. & DENTZ, M. 2017 Anomalous dispersion in correlated porous media: A coupled continuous time random walk approach. *Eur. Phys. J. B* p. accepted.
- COMOLLI, ALESSANDRO, HIDALGO, JUAN J., MOUSSEY, CHARLIE & DENTZ, MARCO 2016 Non-fickian transport under heterogeneous advection and mobile-immobile mass transfer. *Transport in Porous Media* **115** (2), 265–289.
- CVETKOVIC, V. D., DAGAN, G. & SHAPIRO, A. M. 1991 An exact solution of solute transport by one-dimensional random velocity fields. *Stochastic Hydrol. Hydraul.* **5**, 45–54.
- DE ANNA, P., LE BORGNE, T., DENTZ, M., TARTAKOVSKY, A.M., BOLSTER, D. & DAVY, P. 2013 Flow intermittency, dispersion, and correlated continuous time random walks in porous media. *Phys. Rev. Lett.* **110** (18), 184502.
- DE ANNA, P., QUAIFFE, B., BIROS, G. & JUANES, R. 2017 Prediction of velocity distribution from pore structure in simple porous media. *under review* .
- DELAY, F., ACKERER, P. & DANQUIGNY, C. 2005 Simulating solute transport in porous or fractured formations using random walk particle tracking. *Vadose Zone J.* **4**, 360–379.
- DELAY, F., POREL, G. & SARDINI, P. 2002 Modelling diffusion in a heterogeneous rock matrix with a time-domain Lagrangian method and an inversion procedure. *C. R. Geoscience* **334**, 967–973.
- DENTZ, M. & CARRERA, J. 2007 Mixing and spreading in stratified flow. *Phys. Fluids* **19**, 017107.
- DENTZ, M., CORTIS, A., SCHER, H. & BERKOWITZ, B. 2004 Time behavior of solute transport in

- heterogeneous media: transition from anomalous to normal transport. *Adv. Water Resour.* **27** (2), 155–173.
- DENTZ, M., GOUZE, P., RUSSIAN, A., DWEIK, J & DELAY, F. 2012 Diffusion and trapping in heterogeneous media: An inhomogeneous continuous time random walk approach. *Adv. Water Resour.* **49**, 13–22.
- DENTZ, M., KANG, P., COMOLLI, A., LE BORGNE, T. & LESTER, D. R. 2016a Continuous time random walks for the evolution of lagrangian velocities. *Phys. Rev. Fluids* .
- DENTZ, M., LE BORGNE, T., LESTER, D. R. & DE BARROS, F. P. J. 2016b *The Handbook of Groundwater Engineering*, 3rd edn., chap. Mixing in Groundwater, pp. 383–407. Taylor and Francis.
- FELLER, WILLIAM 1968 *An Introduction to Probability and Its Applications Volume I*. John Wiley and Sons.
- FRIEDMAN, G. M. 1962 On sorting, sorting coefficients, and the lognormality of the grain-size distribution of sandstones. *The Journal of Geology* **70**, 737–753.
- GARDINER, C. 2009 *Stochastic Methods*. Springer-Verlag Berlin Heidelberg.
- GJETVAJ, F., RUSSIAN, A., GOUZE, P. & DENTZ, M. 2015 Dual control of flow field heterogeneity and immobile porosity on non-fickian transport in berea sandstone. *Water Resour. Res.* **51**, 8273–8293.
- GOUZE, PH., MELEAN, Z., LE BORGNE, T., DENTZ, M. & CARRERA, J. 2008 Non-fickian dispersion in porous media explained by heterogeneous microscale matrix diffusion. *Water Resour. Res.* **44**, W11416.
- HABER, SHIMON & MAURI, ROBERTO 1988 Lagrangian approach to time-dependent laminar dispersion in rectangular conduits. part 1. two-dimensional flows. *Journal of Fluid Mechanics* **190**, 201–215.
- HAGGERTY, R. & GORELICK, S. M. 1995 Multiple-rate mass transfer for modeling diffusion and surface reactions in media with pore-scale heterogeneity. *Water Resour. Res.* **31** (10), 2383–2400.
- HOLZNER, M., MORALES, V. L., WILLMANN, M. & DENTZ, M. 2015 Intermittent lagrangian velocities and accelerations in three-dimensional porous medium flow. *Phys. Rev. E* **92**, 013015.
- HORNUNG, ULRICH 1997 *Homogenization and Porous Media*. Springer-Verlag New York, Inc.
- ICARDI, MATTEO, BOCCARDO, GIANLUCA, MARCHISIO, DANIELE L, TOSCO, TIZIANA & SETHI, RAJANDREA 2014 Pore-scale simulation of fluid flow and solute dispersion in three-dimensional porous media. *Physical Review E* **90** (1), 013032.
- JIN, C., LANGSTON, P. A., PAVLOVSKAYA, G. E., HALL, M. R. & RIGBY, S. P. 2016 Statistics of highly heterogeneous flow fields confined to three-dimensional random porous media. *Phys. Rev. E* **93**, 013122.
- DE JOSSELYN DE JONG, G. 1958 Longitudinal and transverse diffusion in granular deposits. *Trans. Amer. Geophys. Un.* **39**, 67–74.
- KANG, P. K., DE ANNA, P., NUNES, J.P., BIJELJIC, B., BLUNT, M. J. & JUANES, R. 2014 Pore-scale intermittent velocity structure underpinning anomalous transport through 3-d porous media. *Geophys. Res. Lett.* **41** (17), 6184–6190.
- KENKRE, V. M., MONTROLL, E. W. & SHLESINGER, M. F. 1973 Generalized master equations for continuous-time random walks. *J. Stat. Phys.* **9** (1), 45–50.
- KOPONEN, A, KATAJA, M & TIMONEN, JV 1996 Tortuous flow in porous media. *Physical Review E* **54** (1), 406.
- KREFT, A. & ZUBER, A. 1978 On the physical meaning of the dispersion equation and its solutions for different initial and boundary conditions. *Chem. Eng. Sci.* **33**, 1471–1480.
- LE BORGNE, T., BOLSTER, D., DENTZ, M., DE ANNA, P. & TARTAKOVSKY, A. 2011 Effective pore scale dispersion upscaling with a correlated ctrw approach. *Water Resour. Res.* **47**, W12538.
- LESTER, DR, METCALFE, GUY & TREFRY, MG 2013 Is chaotic advection inherent to porous media flow? *Phys. Rev. Lett.* **111** (17), 174101.
- LESTER, D. R., METCALF, G. & TREFRY, M. G. 2014 Anomalous transport and chaotic advection in homogeneous porous media. *Phys. Rev. E* **90**, 063012.
- LIU, YUAN & KITANIDIS, PETER K 2012 Applicability of the dual-domain model to nonaggregated porous media. *Groundwater* **50** (6), 927–934.

- MARGOLIN, G., DENTZ, M. & BERKOWITZ, B. 2003 Continuous time random walk and multirate mass transfer modeling of sorption. *Chem. Phys.* **295**, 71–80.
- MATYKA, M., GOLEMBIEWSKI, J. & KOZA, Z. 2016 Power-exponential velocity distributions in disordered porous media. *Phys. Rev. E* **93**, 013110.
- MONTROLL, E. W. & WEISS, G. H. 1965 Random walks on lattices, 2. *J. Math. Phys.* **6** (2), 167.
- NOETINGER, BENOIT, ROUBINET, DELPHINE, RUSSIAN, ANNA, LE BORGNE, TANGUY, DELAY, FREDERICK, DENTZ, MARCO, DE DREUZY, JEAN-RAYNALD & GOUZE, PHILIPPE 2016 Random walk methods for modeling hydrodynamic transport in porous and fractured media from pore to reservoir scale. *Transp. Porous Media* pp. 1–41.
- PAINTER, S. & CVETKOVIC, V. 2005 Upscaling discrete fracture network simulations: An alternative to continuum transport models. *Water Resour. Res.* **41**, W02002.
- PFANNKUCH, H. O. 1963 Contribution a l'étude des déplacements de fluides miscibles dans un milieu poreux. *Rev. Inst. Fr. Petr.* **18**, 215–270.
- REDNER, S. 2001 *A Guide to First-Passage Processes*. Cambridge University Press.
- RISKEN, H. 1996 *The Fokker-Planck Equation*. Springer Heidelberg New York.
- RUSSIAN, ANNA, DENTZ, MARCO & GOUZE, PHILIPPE 2016 Time domain random walks for hydrodynamic transport in heterogeneous media. *Water Resources Research* .
- SAFFMAN, PG 1959 A theory of dispersion in a porous medium. *Journal of Fluid Mechanics* **6** (03), 321–349.
- SCHER, H. & LAX, M. 1973 Stochastic transport in a disordered solid. I. Theory. *Phys. Rev. B* **7** (1), 4491–4502.
- SCHEVEN, UM 2013 Pore-scale mixing and transverse dispersivity of randomly packed monodisperse spheres. *Phys. Rev. Lett.* **110** (21), 214504.
- SCHEVEN, UM, HARRIS, R & JOHNS, ML 2007 Intrinsic dispersivity of randomly packed monodisperse spheres. *Physical review letters* **99** (5), 054502.
- SIENA, M, RIVA, M, HYMAN, JD, WINTER, C LARRABEE & GUADAGNINI, A 2014 Relationship between pore size and velocity probability distributions in stochastically generated porous media. *Physical Review E* **89** (1), 013018.
- TAYLOR, G. I. 1953 Dispersion of soluble matter in solvent flowing slowly through a tube. *Proc. R. Soc. Lond. A* **219**, 186–203.
- WHITAKER, S. 1999 *The Method of Volume Averaging*. Kluwer Academic Publishers.